Numerical computation of effective stiffness for spatially graded beam-like structures based on asymptotic homogenization

Liang Xu[a,b] , Yuchi Zhang[a], Degang Zhang[a], Dianzi Liu[c], Zhenghua Qian[a*]

a. State Key Laboratory of Mechanics and Control of Mechanical Structures, College of Aerospace Engineering, Nanjing University of Aeronautics and Astronautics, Nanjing 210016, China

b. State Key Laboratory of Structural Analysis for Industrial Equipment, Dalian University of Technology, Dalian 116024, China

c. School of Engineering, University of East Anglia, UK

Abstract

This work investigates asymptotic homogenization method (AHM) for axially graded beams that are mapped from periodic ones. The unit cell problems, the homogenized constitutive and governing equations are first established theoretically. Then a novel FE formulation of unit cell problems and effective stiffness, distinct from that of the periodic beams, is derived and resolved for solid elements. Besides, to improve analysis efficiency, an updated concise formulation is acquired for shell elements with proper handle of in-plane rotational DOFs, and a MATLAB code is presented to show implementation details. At last, four numerical examples show the correctness of the proposed method.

Keywords: Spatially graded beams, Effective stiffness, Asymptotic homogenization, Numerical implementation, Mapping functions

1. Introduction

Heterogeneous beam structures are ubiquitous in aerospace, transportation and other engineering fields due to their high specific stiffness/strength, high energy absorption, thermal/acoustic insulation and other good performances. With the increasing demand for multi-functionality and the rapid development of the additive manufacturing technique [1], the architectures of beam-like structures with fine configuration details are becoming more and more sophisticated [2,3]. This poses great challenge to their efficient structural analysis and design, as intensive numerical computations are usually inevitable for these structures to acquire satisfactory results through direct numerical analysis. To weigh between computational cost and analysis precision, homogenization approaches are proposed to turn the original

one-scale analysis of heterogeneous structures into two-scale analysis of equivalent homogeneous counterparts with effective properties, which are acquired through analyzing the constituent materials/microstructures.

One kind of frequently employed heterogeneous beam structures are functionally graded (FG) beams with multiphase constituent materials or graded beam sections, whose constituents can be adjusted to achieve specified or extremal performances. Significant efforts have been devoted to the analysis and design of these structures. Garg et al. [4] conducted bending and free vibration analysis of FG CNT reinforced beam, and the influence of CNT gradation and core thickness on mechanical performance is emphasized. Belarbi et al. [5] evaluated FG sandwich curved beams via refined shear deformation theory, and the effect of different factors on the mechanical performances is investigated. For vibration analysis, Cao et al. [6] studied axially FG beams using the asymptotic development method, where influence of gradient parameters and support conditions is discussed. Chen and Su [7] studied the analytical solution of FG sandwich beams using the refined zigzag theory, and Zhao et al. [8] analyzed nonlinear free vibration characteristics for auxetic metamaterial beams. For stability problems, Chen et al. [9] analyzed buckling performances of FG beams based on FE homogenization, and Zhao et al. [10] studied buckling and postbuckling resistance of FG graphene origami-enabled auxetic metamaterial beams. The novel Carrera Unified Formulation (CUF) [11] is another effective analysis framework for beam structures. In CUF, the expansion functions are adopted across the beam cross-section therein to enrich the kinematics, and accurate solutions can be obtained at a reduced computational cost. It has been successfully employed to solve physical [12] and geometrical [13] nonlinear problems. In addition to structural analysis, structural optimization has also been extensively investigated for FG beams. Tsiatas and Charalampakis [14] conducted design optimization of natural frequency by tailoring material distribution, and Andrianov et al.[15] studied maximum buckling load design of FG beams based on the homogenization method. Due to limited space, many other literatures regarding this aspect are not listed here, and interested readers may refer to [16] for modeling techniques and solution methods for FG sandwich beams based on classical and shear deformation theories, and [17] for mechanics of FG nanoscale and microscale structures.

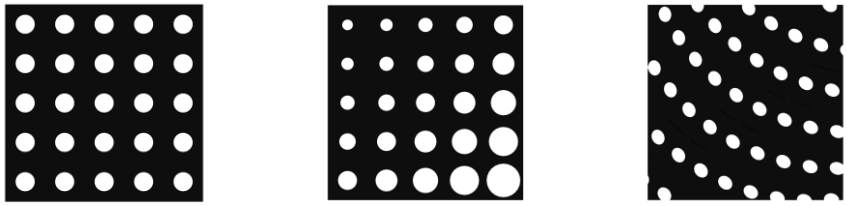

(a). the periodic structure (b). the graded structure by varying cavity radius (c). the graded structure constructed through mapping functions

Figure 1. Sketch of the periodic structure and its spatially graded counterparts

Another kind of commonly employed heterogeneous beam-like structures are constructed by repeating constituent microstructures, which are usually termed as unit cells or representative volume elements (RVE), along the axial direction. The shapes of these structures exhibit rapidly changing characteristics in the micro scale, while display slowly varying deformation patterns in the macro scale. Accordingly, the asymptotic homogenization approach [18], which is originally developed to handle PDEs with oscillating coefficients in mathematics, is an ideal tool in analyzing these structures. In the field of mechanics, the AH approach is first applied to repetitively arranged microstructures with periodicity in all spatial directions, depicted in Figure 1(a), and the heterogeneous structure is homogenized into elastic medium with effective property. It is then extended to heterogeneous plate/shell-like structures with in-plane periodicity [19,20] and beam-like structures with axial periodicity [21-23], which are respectively homogenized into solid Kirchhoff plates/shells and Euler beams with effective stiffness. When computing effective property/stiffness in AH approach, the characteristic displacements, which display different periodic boundary conditions for different homogenized structural models, must be acquired by resolving unit cell problems, which are defined on a typical constituent microstructure. Hence, efficient and accurate solution to unit cell problems is vital for effective property/stiffness evaluation. For unit cells with simple shapes, closed-form solutions can be acquired [24,25], while, for complicated configurations, numerical methods, which are more versatile in handling complex geometries, should be adopted. Cartraud and Messager [26] developed the numerical computational scheme for periodic beam-like structures based on homogenization, and applied it to the analysis of helical strands with solid and beam FE models [27]. Cheng et al. [28] proposed a novel numerical implementation approach of asymptotic homogenization (NIAH) for effective property evaluation of heterogeneous materials. Here, by replacing unit strains with equivalent displacements, the numerical formulation is simplified and the workload of FE coding is significantly relieved. This approach is later extended to periodic plate-like

[29] and beam-like [30] structures, which substantially facilitates widespread application of AH method. Yan et al. [31] analyzed effective properties of helically wound structures based on NIAH, with emphasis on the transverse shear effect. Huo et al. [32] evaluated elastic properties of rhombic mesh structures based on computational homogenization, where numerical effective properties agree well with analytical ones and the struct-joint deformation can be captured by the beam-spring elements.

Besides, the asymptotic expansion method (AEM) [33] is another effective tool in analyzing periodic beam structures by including higher-order terms, where the incompatibility between interior asymptotic expansions and real boundary conditions is emphasized. Treyssede and Cartraud [34] applied AEM to the analysis of helical beam-like structures under bending loads, where the special treatment exploiting helical symmetry is adopted to reduce the original 3D microstructural analysis to 2D cross-section analysis. Ferradi and Cespedes [35] developed a new efficient and locking free beam model from AEM, capable of representing full 3D stresses and the displacement filed, for curved beam models, which is an extension of straight beams [36]. Huang et al. [37] studied fourth-order asymptotic expansion for periodic composite Euler beams and revealed that higher-order perturbed displacements are necessary for accurate micro stress evaluation. It is noted that, in AEM, the higher-order terms can substantially improve analysis precision, yet the unit cell problems related to higher-order terms are quite complicated. Further endeavor needs to be conducted to promote its general numerical application to arbitrarily shaped microstructures.

In addition to the AHM and AEM, where the governing equations are directly asymptotically expanded, the variational asymptotic method (VAM) [38,39] analyzes beam structures through variation of the strain energy that has been asymptotically expanded in terms of small parameters. Generalized from the VAM approach, Yu [40] proposed the mechanics of a structure genome (MSG), aiming at providing a unified framework for multiscale constitutive modeling. Based on MSG, Liu and Yu [41] studied smeared properties and stress evaluations of composite beams, and special software, such as Gmsh4SC and SwiftComp^{TM} [42], is also developed to promote the practical numerical evaluation of constitutive models for beam structures.

In the previous works, beam structures typically exhibit strictly periodic micro architectures. To improve structural performance, the axially varying microstructures, which enjoy more design freedom than periodic ones, offer a sound choice. One direct means of gradation design is to alter gradually microstructural parameters, such as radii and volume fractions, as depicted in Figure 1(b). Here the

effective property can still be approximated through asymptotic analysis in spite of slight inconsistency against the periodic condition. Niknam and Akbarzadeh [43] studied in-plane and out-of-plane buckling of architected cellular plates, where the graded cell densities can help increase buckling loads. Similar advantage is also revealed for graded cellular beams in the thermo-mechanical bending analysis [44], where the bending stiffness can be significantly improved through gradient density design. Liu et al. [45] conducted design optimization of cellular structure with graded relative densities, where a post-process method is proposed to acquire smooth transition boundaries, and Savio et al. [46] studied variable thickness design approaches of triply periodic minimal surfaces (TPMS) in a CAD environment for additive manufacturing.

Another approach of graded cellular design is to project periodic microstructures through mapping functions, as depicted in Figure 1(c). Here the microstructural configurations are no longer rectangular and the effective properties cannot be acquired through previous asymptotic methods. To tackle this problem, Zhu et al. [47] introduced mapping functions into asymptotic analysis of 2D graded microstructures, where the unit cell problems are reformulated incorporating Jacobian coefficients. This approach is then exploited in the design optimization of graded infill microstructures [48]. In a similar manner, Xu et al. [49] developed asymptotic homogenization method for spatially graded plate structures, where detailed numerical resolution of unit cell problems and effective stiffness is elaborated. However, for graded beam structures mapped from periodic ones, the effective properties based on asymptotic homogenization has not been fully exploited. Hence, in this work, the authors are devoted to the analysis of unit cell problems and effective stiffness for axially varying beam structures, where numerical implementation for different element types is investigated.

The rest of the paper is structured as follows. In Section 2, the unit cell problems and effective stiffness formulation of spatially graded beams are derived based on AHM, and are reformulated in a more compact form in Section 3 to facilitate numerical implementation. The FE formulation of unit cell problems and effective stiffness is dealt with in Section 4, for both solid and shell elements. In Section 5, four numerical examples are presented to show the effectiveness of the proposed method, and an 80-line MATLAB code with implementation details is given in Appendix A. At last, conclusions and comments are drawn in Section 6.

2. Asymptotic homogenization for spatially graded beam-like structures

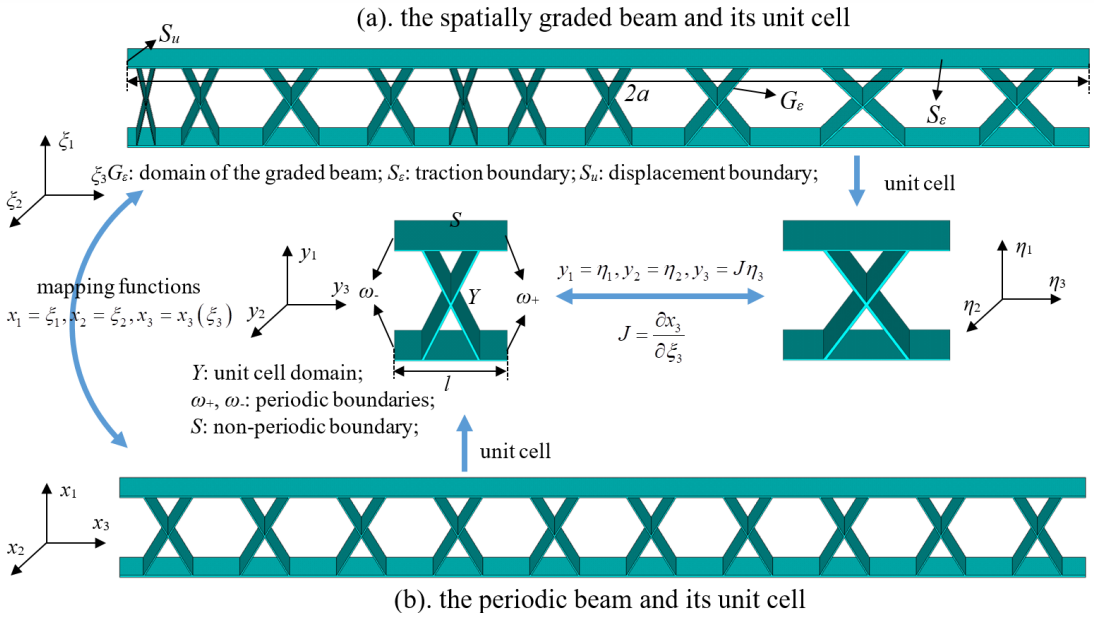

Figure 2. The spatially graded beam-like structure and its periodic counterpart

First, we consider the graded beam-like structure in the $O\xi_1\xi_2\xi_3$ coordinate in Figure 2(a). Here, the domain, the surface traction boundary and the displacement boundary of the graded beam are denoted by Ω_ε, S_ε, and S_u respectively, and the total length is $2a$, varying from ξ_3=-a to ξ_3=a. The graded beam is mapped from the periodic beam-like structure in the $Ox_1x_2x_3$ coordinate in Figure 2(b), and the mapping functions are $x_1=\xi_1, x_2=\xi_2, x_3=x_3(\xi_3)$. The periodic beam structure is constructed by repeating the unit cell along the axial direction, i.e., the x_3 axis, and ε denotes the characteristic dimension of the unit cell, which is much smaller than that of the whole periodic beam. The length, the domain, the non-periodic boundary and the periodic boundary of the unit cell are denoted by l, Y, S and $\omega_\pm$ respectively in the micro $Oy_1y_2y_3$ coordinate, varying from y_3=-l/2 to y_3=l/2. The micro unit cell of the graded beam structure, which is axially varying along the ξ_3 axis, is defined in the $O\eta_1\eta_2\eta_3$ coordinate. The relation between **y** and **η** is given by

$$y_1=\eta_1, y_2=\eta_2, y_3=J\eta_3 \tag{1}$$

where $J=\frac{\partial x_3}{\partial \xi_3}$. In AHM, the macroscopic design variables **x** and **ξ** are termed as slow variables and the microscopic design variables **y** and **η** are termed as fast variables. The relation between slow and fast variables is $\mathbf{y}=\frac{\mathbf{x}(\boldsymbol{\xi})}{\varepsilon}$ and the spatial gradient is given by

$$\frac{\partial}{\partial \xi_\alpha}=\frac{1}{\varepsilon}\frac{\partial}{\partial y_\beta},\frac{\partial}{\partial \xi_3}=\frac{\partial}{\partial \xi_3}+\frac{J}{\varepsilon}\frac{\partial}{\partial y_3} \tag{2}$$

which is similar to that in [47]. Here the Greek subscripts vary from 1 to 2, the Latin subscripts vary from 1 to 3, and the summation convention is adopted for repeated subscripts unless otherwise stated.

The 3D equilibrium equation of the graded beam structure is expressed as

$$\begin{aligned}&\frac{\partial \sigma_{ij}^{\varepsilon}}{\partial \xi_j}+f_i^{\varepsilon}=0 \quad \text{in } G_\varepsilon\\&\sigma_{ij}^{\varepsilon}N_j=g_i^{\varepsilon} \quad \text{on } S_\varepsilon\\&u_m^{\varepsilon}=0 \quad \text{on } S_u\end{aligned} \tag{3}$$

Here $\sigma_{ij}^{\varepsilon}=c_{ijkl}\varepsilon_{kl}^{\varepsilon},\varepsilon_{kl}^{\varepsilon}=\frac{1}{2}\left(\frac{\partial u_k^{\varepsilon}}{\partial \xi_l}+\frac{\partial u_l^{\varepsilon}}{\partial \xi_k}\right)$, $\boldsymbol{\sigma}^{\varepsilon}$ denotes the oscillatory stress tensor, $\mathbf{u}^{\varepsilon}$ denotes the oscillatory displacement, $\boldsymbol{\varepsilon}^{\varepsilon}$ denotes the oscillatory strain, $\mathbf{c}$ denotes the elastic tensor satisfying the periodic condition $\mathbf{c}\left(x_1,x_2,x_3\right)=\mathbf{c}\left(x_1,x_2,x_3+\varepsilon Ml\right)$ with arbitrary integers M, $\mathbf{N}$ is the unit outward normal, and $\mathbf{f}^{\varepsilon}$ and $\mathbf{g}^{\varepsilon}$ are the prescribed body force in Ω^{ε} and tractions on S_ε, which are written in the orders of ε as

$$\mathbf{f}^{\varepsilon}=\left\{\varepsilon^2 f_1 \quad \varepsilon^2 f_2 \quad \varepsilon^1 f_3\right\}^{\mathrm{T}}\left(\xi_3,\mathbf{x}/\varepsilon\right),\mathbf{g}^{\varepsilon}=\left\{\varepsilon^3 g_1 \quad \varepsilon^3 g_2 \quad \varepsilon^2 g_3\right\}^{\mathrm{T}}\left(\xi_3,\mathbf{x}/\varepsilon\right) \tag{4}$$

The displacement field $\mathbf{u}^{\varepsilon}$ is expanded asymptotically as

$$\mathbf{u}^{\varepsilon}\left(\boldsymbol{\xi}\right)=\mathbf{u}^{(0)}\left(\xi_3\right)+\varepsilon\mathbf{u}^{(1)}\left(\xi_3,\mathbf{y}\right)+\varepsilon^2\mathbf{u}^{(2)}\left(\xi_3,\mathbf{y}\right)+\cdots \tag{5}$$

where $\mathbf{u}^{(p)}$ are periodic functions in y_3 with periodicity unit cell length l. Then the stress tensor $\boldsymbol{\sigma}^{\varepsilon}$ can be expanded as

$$\sigma_{ij}^{\varepsilon}=\sum_{p=-1}^{\infty}\varepsilon^p\sigma_{ij}^{(p)},\sigma_{ij}^{(p)}=c_{ijk3}\frac{\partial u_k^{(p)}}{\partial \xi_3}+c_{ijkl}J_{nl}\frac{\partial u_k^{(p+1)}}{\partial y_n},\left(p\geq 0\right) \tag{6}$$

where J_{nl} is the coefficients of the Jacobian matrix $\mathbf{J}$, given by $\mathbf{J}=\left[\partial x_i/\partial \xi_j\right]_{3\times 3}=\begin{bmatrix}1&0&0\\0&1&0\\0&0&J\end{bmatrix}$.

Then following the procedure in [22], we introduce the trial function $\mathbf{v}^{\varepsilon}$, which is the set of admissible displacements satisfying the displacement boundary condition $\mathbf{v}^{\varepsilon}\big|_{S_u}=\mathbf{0}$, to study the homogenized equilibrium equation. The weak form of Eq. is given by

$$\int_{G_\varepsilon}\sigma_{ij}^{\varepsilon}\frac{\partial v_i^{\varepsilon}}{\partial \xi_j}d\boldsymbol{\xi}=\int_{S_\varepsilon}\mathbf{g}^{\varepsilon}\mathbf{v}^{\varepsilon}d\boldsymbol{\xi}+\int_{G_\varepsilon}\mathbf{f}^{\varepsilon}\mathbf{v}^{\varepsilon}d\boldsymbol{\xi} \tag{7}$$

Substituting

is expanded as

$$\sum_{p=0}^{\infty}\int_{G_\varepsilon}\left[\varepsilon^p\sigma_{i3}^{(p)}\frac{\partial v_i^\varepsilon}{\partial\xi_3}+\varepsilon^{p-1}J_{nl}\sigma_{in}^{(p)}\frac{\partial v_i^\varepsilon}{\partial y_l}\right]d\boldsymbol{\xi}$$
$$=\varepsilon^3\int_{S_\varepsilon}g_\alpha^\varepsilon v_\alpha^\varepsilon d\boldsymbol{\xi}+\varepsilon^2\int_{S_\varepsilon}g_3^\varepsilon v_3^\varepsilon d\boldsymbol{\xi}+\varepsilon^2\int_{G_\varepsilon}f_\alpha^\varepsilon v_\alpha^\varepsilon d\boldsymbol{\xi}+\varepsilon^1\int_{G_\varepsilon}f_3^\varepsilon v_3^\varepsilon d\boldsymbol{\xi}$$

Letting $\mathbf{v}^\varepsilon=\mathbf{w}(\xi_3)$ and $\varepsilon\to 0$, Eq.

$$\sum_{p=0}^{\infty}\int_{-a}^{a}\varepsilon^{p+2}N_{i3}^{(p)}\frac{\partial w_i}{\partial\xi_3}d\xi_3=\varepsilon^4\int_{-a}^{a}\left\langle g_\alpha^\varepsilon\right\rangle_S w_\alpha d\xi_3+\varepsilon^3\int_{-a}^{a}\left\langle g_3^\varepsilon\right\rangle_S w_3 d\xi_3+\varepsilon^4\int_{-a}^{a}\left\langle f_\alpha^\varepsilon\right\rangle w_\alpha d\xi_3+\varepsilon^3\int_{-a}^{a}\left\langle f_3^\varepsilon\right\rangle w_3 d\xi_3$$

(9)

where $N_{ij}^{(p)}=\left\langle\sigma_{ij}^{(p)}\right\rangle$, $\langle\ \rangle=\frac{1}{l}\int_Y d\mathbf{y}$ and $\langle\ \rangle_S=\frac{1}{l}\int_S d\mathbf{y}$. Then an infinite set of equilibrium equations for $N_{ij}^{(p)}$ is obtained from Eq.

extracted as

$$\varepsilon^2:\int_{-a}^{a}N_{i3}^{(p)}\frac{\partial w_i}{\partial\xi_3}d\xi_3=0$$
$$\varepsilon^3:\int_{-a}^{a}N_{i3}^{(1)}\frac{\partial w_i}{\partial\xi_3}d\xi_3=\int_{-a}^{a}\left\langle g_3^\varepsilon\right\rangle_S w_3 d\xi_3+\int_{-a}^{a}\left\langle f_3^\varepsilon\right\rangle w_3 d\xi_3$$
$$\varepsilon^4:\int_{-a}^{a}N_{i3}^{(2)}\frac{\partial w_i}{\partial\xi_3}d\xi_3=\int_{-a}^{a}\left(\left\langle g_\alpha^\varepsilon\right\rangle_S+\left\langle f_\alpha^\varepsilon\right\rangle\right)w_\alpha d\xi_3$$

Integrating by parts and considering the arbitrariness of the displacement **w**, the homogenized equilibrium equations for $N_{ij}^{(p)}$ are obtained as

$$\frac{\partial N_{i3}^{(0)}}{\partial\xi_3}=0,\frac{\partial N_{33}^{(1)}}{\partial\xi_3}+\left\langle g_3^\varepsilon\right\rangle_S+\left\langle f_3^\varepsilon\right\rangle=0,\frac{\partial N_{\alpha3}^{(2)}}{\partial\xi_3}+\left\langle g_\alpha^\varepsilon\right\rangle_S+\left\langle f_\alpha^\varepsilon\right\rangle=0$$

On the other hand, letting $\mathbf{v}=y_\beta\mathbf{w}(\xi_3)$ and substituting **v** into Eq.(8) Eq.(8) is transformed into the following equality by setting $\varepsilon\to 0$

$$\sum_{p=0}^{\infty}\int_{-a}^{a}\left(\varepsilon^{p+2}M_{i\beta}^{(p)}\frac{\partial w_i}{\partial\xi_3}+\varepsilon^{p+1}N_{i\beta}^{(p)}w_i\right)d\xi_3$$
$$=\varepsilon^4\int_{-a}^{a}\left\langle g_\alpha^\varepsilon y_\beta\right\rangle_S w_\alpha d\xi_3+\varepsilon^3\int_{-a}^{a}\left\langle g_3^\varepsilon y_\beta\right\rangle_S w_3 d\xi_3+\varepsilon^4\int_{-a}^{a}\left\langle f_\alpha^\varepsilon y_\beta\right\rangle w_\alpha d\xi_3+\varepsilon^3\int_{-a}^{a}\left\langle f_3^\varepsilon y_\beta\right\rangle w_3 d\xi_3$$

where $M_{i\beta}^{(p)}=\left\langle\sigma_{i3}^{(p)}y_\beta\right\rangle$. Extracting the terms related to ε^1, ε^2 and ε^3, integrating by parts and consider the arbitrariness of **w**, the homogenized equilibrium equations for $M_{i\beta}^{(p)}$ are obtained as

$$N_{i\beta}^{(0)}=0,\frac{\partial M_{i\beta}^{(0)}}{\partial x_3}-N_{i\beta}^{(1)}=0,\frac{\partial M_{i\beta}^{(1)}}{\partial x_3}-N_{i\beta}^{(2)}+\delta_{i3}\left(\left\langle g_3^\varepsilon y_\beta\right\rangle_S+\left\langle f_3^\varepsilon y_\beta\right\rangle\right)=0 \qquad (13)$$

Define the torsional moment M as $M = M_{21}^{(1)} - M_{12}^{(1)} = e_{\alpha\beta 3} M_{\beta\alpha}^{(1)} = \left\langle e_{\alpha\beta 3} \sigma_{\beta 3}^{(1)} y_\alpha \right\rangle$, where $e_{\alpha\beta 3}$ is the alternating symbol. Then the last equality in Eq. is expanded as

$$\frac{\partial M_{3\beta}^{(1)}}{\partial x_3} - N_{3\beta}^{(2)} + \left\langle g_3^\varepsilon y_\beta \right\rangle_S + \left\langle f_3^\varepsilon y_\beta \right\rangle = 0, \frac{\partial M}{\partial x_3} = 0 \tag{14}$$

where we have used the relation $N_{12}^{(2)} = N_{21}^{(2)}$.

Next, consider equilibrium equations in the micro scale. Substituting Eq.

collating the terms with the same powers of the small parameter ε, Eq. is expanded as

$$\begin{aligned} &\varepsilon^{-1} J_{nj} \frac{\partial \sigma_{ij}^{(0)}}{\partial y_n} + \varepsilon^0 \left(\frac{\partial \sigma_{i3}^{(0)}}{\partial \xi_3} + J_{nj} \frac{\partial \sigma_{ij}^{(1)}}{\partial y_n} \right) + \cdots + f_i^\varepsilon = 0 \ \text{ in } G_\varepsilon \\ &\varepsilon^0 \sigma_{ij}^{(0)} J_{pj} n_j + \varepsilon^1 \sigma_{ij}^{(1)} J_{pj} n_j + \cdots = g_i^\varepsilon \ \text{ on } S_\varepsilon \end{aligned} \tag{15}$$

where **n** is the unit outward normal in the $Oy_1y_2y_3$ coordinate.

Using the method of separation of variables, assume that the solution of displacement $u_k^{(1)}$ can be written as $u_k^{(1)}(\xi_3, \mathbf{y}) = X_k^{0m}(\mathbf{y}) \frac{\partial u_m^{(0)}}{\partial \xi_3} + v_k^{(1)}(\xi_3) + e_{\alpha\beta 3} y_\alpha \delta_{\beta k} \phi(x_3)$ [22], where $X_k^{0m}(\mathbf{y})$ is the periodic function in y_3 with periodicity unit cell length l. Then the governing equations corresponding to the lowest order of ε are given by

$$\begin{cases} J_{pj} \dfrac{\partial}{\partial y_p} \left(c_{ijkl} J_{nl} \dfrac{\partial X_k^{0m}}{\partial y_n} + c_{ijm3} \right) = 0 \ \text{ in } Y \\ \left(c_{ijkl} J_{nl} \dfrac{\partial X_k^{0m}}{\partial y_n} + c_{ijm3} \right) J_{pj} n_p = 0 \ \text{ on } S \end{cases} \tag{16}$$

It is easy to deduce that, for $m=\alpha$, X_k^{0m} has the solution $X_k^{0\alpha} = -y_\alpha \delta_{k3}$ and $u_k^{(1)}$ can be expressed as $u_k^{(1)} = -y_\alpha \delta_{k3} \frac{\partial u_\alpha^{(0)}}{\partial \xi_3} + X_k^{03} \frac{\partial u_3^{(0)}}{\partial \xi_3} + e_{\alpha\beta 3} y_\alpha \delta_{\beta k} \phi(x_3) + v_k^{(1)}(\xi_3)$. Hence 0-th order stress is given by $\sigma_{ij}^{(0)} = \left(c_{ijkl} J_{nl} \frac{\partial X_k^{03}}{\partial y_n} + c_{ij33} \right) \frac{\partial u_3^{(0)}}{\partial \xi_3}$. Substitute $\sigma_{ij}^{(0)}$ into homogenized governing equations, and we obtain $\left\langle c_{33kl} J_{nl} \frac{\partial X_k^{03}}{\partial y_n} + c_{3333} \right\rangle \frac{\partial^2 u_3^{(0)}}{\partial x_3^2} = 0, u_3^{(0)}(-a) = u_3^{(0)}(a) = 0$. Therefore $u_3^{(0)} = 0$, $\sigma_{ij}^{(0)} = 0$ and $N_{ij}^{(0)} = 0$.

The governing equations corresponding to ε^0 are written as

$$\begin{cases} J_{pj}\dfrac{\partial}{\partial y_p}\left(c_{ijk3}\dfrac{\partial u_k^{(1)}}{\partial \xi_3}+c_{ijkl}J_{nl}\dfrac{\partial u_k^{(2)}}{\partial y_n}\right)=0 \ \text{ in } Y \\ \left(c_{ijk3}\dfrac{\partial u_k^{(1)}}{\partial \xi_3}+c_{ijkl}J_{nl}\dfrac{\partial u_k^{(2)}}{\partial y_n}\right)J_{pj}n_p=0 \ \text{ on } S \end{cases} \tag{17}$$

Analogously assume that $u_k^{(2)}$ has the following form of solution

$$u_k^{(2)}=-X_k^{1\alpha}\frac{\partial^2 u_\alpha^{(0)}}{\partial x_3^2}-y_\alpha\delta_{k3}\frac{\partial v_\alpha^{(1)}}{\partial x_3}+X_k^{03}\frac{\partial v_3^{(1)}}{\partial x_3}+X_k^{3}\frac{\partial \phi}{\partial x_3}+e_{\alpha\beta3}y_\alpha\delta_{\beta k}\psi\left(x_3\right)+v_k^{(2)}\left(x_3\right) \tag{18}$$

Then Eq. is expanded as

$$\begin{aligned} &J_{pj}\frac{\partial}{\partial y_p}\left(c_{ijkl}J_{nl}\frac{\partial X_k^{1\alpha}}{\partial y_n}+y_\alpha c_{ij33}\right)\left(-\frac{\partial^2 u_\alpha^{(0)}}{\partial \xi_3^2}\right)+J_{pj}\frac{\partial}{\partial y_p}\left(c_{ijkl}J_{nl}\frac{\partial X_k^{03}}{\partial y_n}+c_{ij33}\right)\frac{\partial v_3^{(1)}}{\partial \xi_3}+J_{pj}\frac{\partial}{\partial y_p}\left(c_{ijkl}J_{nl}\frac{\partial X_k^{3}}{\partial y_n}+c_{ij\beta3}e_{\alpha\beta3}y_\alpha\right)\frac{\partial \phi}{\partial \xi_3}=0 \ \text{ in } Y \\ &\left(c_{ijkl}J_{nl}\frac{\partial X_k^{1\alpha}}{\partial y_n}+y_\alpha c_{ij33}\right)J_{pj}n_p\left(-\frac{\partial^2 u_\alpha^{(0)}}{\partial \xi_3^2}\right)+\left(c_{ijkl}J_{nl}\frac{\partial X_k^{03}}{\partial y_n}+c_{ij33}\right)J_{pj}n_p\frac{\partial v_3^{(1)}}{\partial \xi_3}+\left(c_{ijkl}J_{nl}\frac{\partial X_k^{3}}{\partial y_n}+c_{ij\beta3}e_{\alpha\beta3}y_\alpha\right)J_{pj}n_p\frac{\partial \phi}{\partial \xi_3}=0 \ \text{ on } S \end{aligned} \tag{19}$$

For the sake of brevity, defining the terms $b_{ij}^{03}=c_{ijkl}J_{nl}\dfrac{\partial X_k^{03}}{\partial y_n}+c_{ij33}$, $b_{ij}^{1\alpha}=c_{ijkl}J_{nl}\dfrac{\partial X_k^{1\alpha}}{\partial y_n}+y_\alpha c_{ij33}$, $b_{ij}^{3}=c_{ijkl}J_{nl}\dfrac{\partial X_k^{3}}{\partial y_n}+c_{ij\beta3}e_{\alpha\beta3}y_\alpha$, and considering the arbitrariness of macro deformations $-\dfrac{\partial^2 u_\alpha^{(0)}}{\partial \xi_3^2},\dfrac{\partial v_3^{(1)}}{\partial \xi_3},\dfrac{\partial \phi}{\partial \xi_3}$, the following governing equations can be acquired through Eq.(as

$$\begin{cases} J_{pj}\dfrac{\partial b_{ij}^{1\alpha}}{\partial y_p}=0 \ \text{ in } Y \\ b_{ij}^{\alpha}J_{pj}n_p=0 \ \text{ on } S \end{cases},\begin{cases} J_{pj}\dfrac{\partial b_{ij}^{03}}{\partial y_p}=0 \ \text{ in } Y \\ b_{ij}^{0}J_{pj}n_p=0 \ \text{ on } S \end{cases},\begin{cases} J_{pj}\dfrac{\partial b_{ij}^{3}}{\partial y_p}=0 \ \text{ in } Y \\ b_{ij}^{3}J_{pj}n_p=0 \ \text{ on } S \end{cases} \tag{20}$$

which are termed as unit cell problems in AHM.

The 1-st order stress $\sigma_{ij}^{(1)}$ is accordingly expressed as $\sigma_{ij}^{(1)}=b_{ij}^{03}\dfrac{\partial v_3^{(1)}}{\partial \xi_3}+b_{ij}^{1\alpha}\left(-\dfrac{\partial^2 u_\alpha^{(0)}}{\partial \xi_3^2}\right)+b_{ij}^{3}\dfrac{\partial \phi}{\partial \xi_3}$.

Substituting $\sigma_{ij}^{(1)}$ into the homogenized resultant forces $N_{33}^{(1)}$, $M_{3\beta}^{(1)}$ and M, the homogenized constitutive relations are expressed as

$$\begin{aligned} N_{33}^{(1)}&=\left\langle b_{33}^{03}\right\rangle\frac{\partial v_3^{(1)}}{\partial \xi_3}+\left\langle b_{33}^{1\alpha}\right\rangle\left(-\frac{\partial^2 u_\alpha^{(0)}}{\partial \xi_3^2}\right)+\left\langle b_{33}^{3}\right\rangle\frac{\partial \phi}{\partial \xi_3} \\ M_{3\beta}^{(1)}&=\left\langle y_\beta b_{33}^{03}\right\rangle\frac{\partial v_3^{(1)}}{\partial \xi_3}+\left\langle y_\beta b_{33}^{1\alpha}\right\rangle\left(-\frac{\partial^2 u_\alpha^{(0)}}{\partial \xi_3^2}\right)+\left\langle y_\beta b_{33}^{3}\right\rangle\frac{\partial \phi}{\partial \xi_3} \\ M&=\left\langle e_{\alpha\beta3}y_\alpha b_{\beta3}^{03}\right\rangle\frac{\partial v_3^{(1)}}{\partial \xi_3}+\left\langle e_{\alpha\beta3}y_\alpha b_{\beta3}^{1\alpha}\right\rangle\left(-\frac{\partial^2 u_\alpha^{(0)}}{\partial \xi_3^2}\right)+\left\langle e_{\alpha\beta3}y_\alpha b_{\beta3}^{3}\right\rangle\frac{\partial \phi}{\partial \xi_3} \end{aligned} \tag{21}$$

Here $N_{33}^{(1)}$, $M_{3\beta}^{(1)}$ and M denote the resultant axial force, the bending moment and the torque respectively. $\frac{\partial v_3^{(1)}}{\partial \xi_3}$, $-\frac{\partial^2 u_\alpha^{(0)}}{\partial \xi_3^2}$ and $\frac{\partial \phi}{\partial \xi_3}$ represent the axial strain, the bending curvature and the torsional strain respectively.

Besides, bearing in mind that $N_{ij}^{(0)} = 0$, the homogenized governing equations are obtained from Eqs.

$$\begin{aligned} &\frac{\partial N_{33}^{(1)}}{\partial \xi_3} + \left\langle g_3^\varepsilon \right\rangle_S + \left\langle f_3^\varepsilon \right\rangle = 0, \frac{\partial M}{\partial \xi_3} = 0 \\ &\frac{\partial^2 M_{3\beta}^{(1)}}{\partial \xi_3^2} + \frac{\partial \left\langle g_\alpha^\varepsilon \right\rangle_S}{\partial \xi_3} + \frac{\partial \left\langle f_\alpha^\varepsilon \right\rangle}{\partial \xi_3} + \left\langle g_3^\varepsilon y_\beta \right\rangle_S + \left\langle f_3^\varepsilon y_\beta \right\rangle = 0 \end{aligned} \tag{22}$$

Therefore, the unit cell problems , the homogenized constitutive equations and the homogenized governing equations are established for the spatially graded beam structures.

3. Equivalent forms of effective stiffness formulation for spatially graded beam structures

In this section, equivalent forms of effective stiffness formulation and unit cell problems are presented in detail to facilitate further FE numerical implementation. First, to collate the unit cell problems in a unified form, the following strains $\varepsilon_{kl}^p \left(p = 1,2,3,4\right)$ are introduced as

$$\varepsilon_{kl}^1 = \delta_{k3}\delta_{l3}, \varepsilon_{kl}^2 = y_1\delta_{k3}\delta_{l3}, \varepsilon_{kl}^3 = y_2\delta_{k3}\delta_{l3}, \varepsilon_{kl}^4 = \frac{1}{2}\left(\delta_{k\beta}\delta_{l3} + \delta_{k3}\delta_{l\beta}\right)e_{\alpha\beta 3}y_\alpha \tag{23}$$

Here δ is the Kronecker δ and Eq.(can be cast into matrix form as

$$\boldsymbol{\varepsilon} = \begin{Bmatrix} \varepsilon_{11} \\ \varepsilon_{22} \\ \varepsilon_{33} \\ \gamma_{12} \\ \gamma_{23} \\ \gamma_{13} \end{Bmatrix}, \boldsymbol{\varepsilon}^1 = \begin{Bmatrix} 0 \\ 0 \\ 1 \\ 0 \\ 0 \\ 0 \end{Bmatrix}, \boldsymbol{\varepsilon}^2 = \begin{Bmatrix} 0 \\ 0 \\ y_1 \\ 0 \\ 0 \\ 0 \end{Bmatrix}, \boldsymbol{\varepsilon}^3 = \begin{Bmatrix} 0 \\ 0 \\ y_2 \\ 0 \\ 0 \\ 0 \end{Bmatrix}, \boldsymbol{\varepsilon}^4 = \begin{Bmatrix} 0 \\ 0 \\ 0 \\ 0 \\ y_1 \\ -y_2 \end{Bmatrix} \tag{24}$$

where $\boldsymbol{\varepsilon}^1$ denotes unit tensile strain, $\boldsymbol{\varepsilon}^2$, $\boldsymbol{\varepsilon}^3$ denote two unit curvatures and $\boldsymbol{\varepsilon}^4$ denotes unit torsional strain. Furthermore, the displacements $\mathbf{U}^1, \mathbf{U}^2, \mathbf{U}^3, \mathbf{U}^4$ are introduced to replace $\mathbf{X}^{03}, \mathbf{X}^{11}, \mathbf{X}^{12}, \mathbf{X}^3$ respectively, and $\mathbf{b}^1, \mathbf{b}^2, \mathbf{b}^3, \mathbf{b}^4$ to replace $\mathbf{b}^{03}, \mathbf{b}^{11}, \mathbf{b}^{12}, \mathbf{b}^3$ respectively in Eqs.

Then $\mathbf{b}^p$ takes the form $b_{ij}^p = c_{ijkl} J_{ql} \dfrac{\partial U_k^p}{\partial y_q} + c_{ijkl} \varepsilon_{kl}^p \left(p = 1,2,3,4 \right)$, and the unit cell problems are recast in a unified manner as

$$\begin{cases} J_{qj} \dfrac{\partial b_{ij}^p}{\partial y_q} = 0 \ \text{ in } Y \\ b_{ij}^p J_{qj} n_q = 0 \ \text{ on } S \\ U_i^p \big|_{\omega_+} = U_i^p \big|_{\omega_-} \ \text{ on } \omega_\pm \\ b_{ij}^p J_{qj} n_q \big|_{\omega_+} = b_{ij}^p J_{qj} n_q \big|_{\omega_-} \ \text{ on } \omega_\pm \end{cases} \tag{25}$$

Here the periodic boundary conditions are obtained from the periodicity of displacements $\mathbf{U}^p \left(p = 1,2,3,4 \right)$ and are presented in Eq.(25) for completeness sake. The effective stiffness in constitutive equation (21) is rearranged as $D^{pq} = \left\langle \varepsilon_{ij}^p b_{ij}^q \right\rangle \left(p,q = 1,2,3,4 \right)$. In addition, considering the periodicity of displacements $\mathbf{U}^p$ (p=1,2,3,4), D^{pq} (p,q=1,2,3,4) can be alternatively cast in energy form as

$$D^{pq} = \left\langle \left(\varepsilon_{ij}^p + J_{mj} \frac{\partial U_i^p}{\partial y_m} \right) b_{ij}^q \right\rangle = \left\langle \left(\varepsilon_{ij}^p + J_{mj} \frac{\partial U_i^p}{\partial y_m} \right) c_{ijkl} \left(\varepsilon_{kl}^q + J_{nl} \frac{\partial U_k^q}{\partial y_n} \right) \right\rangle \tag{26}$$

It is observed that the main difference between the unit cell problems and effective stiffness formulation of graded beam structures and those of the periodic beams is the Jacobian matrix **J**, which induces distinct numerical treatments subsequently.

For periodic beam structures, where **J** reduces to the identity matrix, direct numerical resolution of unit cell problems involves element-wise application of the strain fields (24). In NIAH approach [30] the application of strain fields is replaced with the application of equivalent displacement fields, which is more convenient to fulfill on FE model. For spatially graded beams, this approach can be carried out in an analogous manner and the following displacement fields, defined in the $O\eta_1\eta_2\eta_3$ coordinate, are given by

$$\mathbf{V}^1 = \begin{Bmatrix} 0 \\ 0 \\ y_3/J \end{Bmatrix}, \mathbf{V}^2 = \begin{Bmatrix} -y_3^2/\left(2J^2\right) \\ 0 \\ y_3 y_1/J \end{Bmatrix}, \mathbf{V}^3 = \begin{Bmatrix} 0 \\ -y_3^2/\left(2J^2\right) \\ y_3 y_2/J \end{Bmatrix}, \mathbf{V}^4 = \begin{Bmatrix} -y_2 y_3/J \\ y_1 y_3/J \\ 0 \end{Bmatrix} \tag{27}$$

which satisfy the equality $c_{ijmn}J_{qn}\dfrac{\partial V_m^p}{\partial y_q}=c_{ijmn}\varepsilon_{mn}^p$. The effective stiffness coefficients in Eq. (26) then become $D^{pq}=\left\langle J_{mj}\dfrac{\partial\left(U_i^p+V_i^p\right)}{\partial y_m}c_{ijkl}J_{nl}\dfrac{\partial\left(U_k^q+V_k^q\right)}{\partial y_n}\right\rangle,\left(p,q=1,2,3,4\right)$. Hence the effective stiffness is in effect determined through the sum of displacements $\mathbf{U}^p$ and $\mathbf{V}^p$, and we can alter the unit cell problems to directly seek for the solution of the summation displacements $\mathbf{W}^p=\mathbf{U}^p+\mathbf{V}^p\left(p=1,2,3,4\right)$. Substitute $\mathbf{U}^p=\mathbf{W}^p-\mathbf{V}^p$ into Eq.(25), and the modified unit cell problems are stated as

$$\begin{cases} J_{qj}\dfrac{\partial}{\partial y_q}\left(c_{ijkl}J_{ml}\dfrac{\partial W_k^p}{\partial y_m}\right)=0 \ \text{ in } Y \\ c_{ijkl}J_{ml}\dfrac{\partial W_k^p}{\partial y_m}J_{qj}n_q=0 \ \text{ on } S \\ W_i^p\big|_{\omega_+}-W_i^p\big|_{\omega_-}=\Delta V_i^p \ \text{ on } \omega_\pm \\ c_{ijkl}J_{ml}\dfrac{\partial W_k^p}{\partial y_m}J_{qj}n_q\Big|_{\omega_+}=c_{ijkl}J_{ml}\dfrac{\partial W_k^p}{\partial y_m}J_{qj}n_q\Big|_{\omega_-} \ \text{ on } \omega_\pm \end{cases} \tag{28}$$

Here we have used the relation $c_{ijkl}J_{ml}\dfrac{\partial V_k^p}{\partial y_m}J_{qj}n_q\Big|_{\omega_+}=c_{ijkl}J_{ml}\dfrac{\partial V_k^p}{\partial y_m}J_{qj}n_q\Big|_{\omega_-}$ on $\omega_\pm$, and $\Delta\mathbf{V}^p=\mathbf{V}^p\big|_{\omega_+}-\mathbf{V}^p\big|_{\omega_-}$ is given by

$$\Delta\mathbf{V}^1=\begin{Bmatrix}0\\0\\l/J\end{Bmatrix},\Delta\mathbf{V}^2=\begin{Bmatrix}0\\0\\ly_1/J\end{Bmatrix},\Delta\mathbf{V}^3=\begin{Bmatrix}0\\0\\ly_2/J\end{Bmatrix},\Delta\mathbf{V}^4=\begin{Bmatrix}-ly_2/J\\ly_1/J\\0\end{Bmatrix} \tag{29}$$

The stiffness coefficients are hence written as

$$D^{pq}=\left\langle\left(J_{mj}\frac{\partial W_i^p}{\partial y_m}\right)c_{ijkl}\left(J_{nl}\frac{\partial W_k^q}{\partial y_n}\right)\right\rangle,\left(p,q=1,2,3,4\right) \tag{30}$$

It is noted that the displacement boundary condition of $\mathbf{W}^p$ only involves the displacement value $\mathbf{V}^p$ on ω_+ and ω- boundary, and the values of $\mathbf{V}^p$ inside the unit cell do not influence the displacement boundary condition. Besides, for the special case of periodic beam structures, the unit cell problems and effective stiffness formulation can be readily obtained by setting $J_{mn}=\delta_{mn}$ in Eqs.

4. Numerical implementation of unit cell problems and effective stiffness formulation

In this section, the numerical formulation of the unit cell problems (28) and effective stiffness (30) are derived in detail for both solid and shell elements, where the numerical treatments in the derivation of rotational DOFs (Degrees of Freedom) are emphasized.

4.1 Effective stiffness and unit cell problem formulation for solid elements

To construct the FE formulation for the unknown displacements $\mathbf{W}^p$ in Eq.(28), the trial function $\mathbf{v}$ which fulfills the periodic boundary condition $\mathbf{v}|_{\omega_+} = \mathbf{v}|_{\omega_-}$, is introduced. The weak form of the unit cell problems becomes

$$\int_Y v_i J_{qj} \frac{\partial}{\partial y_q}\left(c_{ijkl} J_{ml} \frac{\partial W_k^p}{\partial y_m} \right) d\Omega - \int_S v_i c_{ijkl} J_{ml} \frac{\partial W_k^p}{\partial y_m} J_{qj} n_q dA - \int_{\omega_\pm} v_i c_{ijkl} J_{ml} \frac{\partial W_k^p}{\partial y_m} J_{qj} n_q dA = 0 \tag{31}$$

Integrating by parts and letting $\mathbf{v}$ be the variation of the displacement $\mathbf{W}^p$, Eq.(31) is expressed through the divergence theorem as

$$\int_Y \delta\bar{\varepsilon}_{ij}^p c_{ijkl} \bar{\varepsilon}_{kl}^p d\mathbf{y} = 0 \tag{32}$$

Here the repeated superscript p is not summed up and $\bar{\varepsilon}_{ij}^p = \frac{1}{2}\left(J_{pj} \frac{\partial W_i^p}{\partial y_p} + J_{pi} \frac{\partial W_j^p}{\partial y_p} \right)$, which is distinct from conventional strains and is distinguished with an overbar. Then following the standard FEM procedure, we discretize the unit cell into n_e solid elements and the discrete form of Eq.(32 is given by

$$\sum_{e=1}^{n_e} \delta\left({}^{\mathrm{n}}\mathbf{W}_e^p \right)^{\mathrm{T}} \mathbf{k}_e {}^{\mathrm{n}}\mathbf{W}_e^p = 0 \tag{33}$$

Here the right subscript e denotes e-th element, the left superscript n signifies discretized nodal values, ${}^{\mathrm{n}}\mathbf{W}_e^p$ denotes the displacement vector of e-th element, and $\mathbf{k}_e$ denotes the stiffness matrix of e-th element, given by

$$\mathbf{k}_e = \int_{\Omega_e} \left[\bar{\mathbf{B}}(\mathbf{y}) \right]^{\mathrm{T}} \mathbf{c} \bar{\mathbf{B}}(\mathbf{y}) d\mathbf{y} \tag{34}$$

Here Ω_e denotes the domain of e-th element, and the strain-displacement matrix $\bar{\mathbf{B}}(\mathbf{y})$ is defined through the following equation

$$\begin{Bmatrix} \bar{\varepsilon}_{11} \\ \bar{\varepsilon}_{22} \\ \bar{\varepsilon}_{33} \\ 2\bar{\varepsilon}_{12} \\ 2\bar{\varepsilon}_{23} \\ 2\bar{\varepsilon}_{31} \end{Bmatrix} = \begin{bmatrix} 1 & 0 & 0 & 0 & 0 & 0 & 0 & 0 & 0 \\ 0 & 1 & 0 & 0 & 0 & 0 & 0 & 0 & 0 \\ 0 & 0 & J & 0 & 0 & 0 & 0 & 0 & 0 \\ 0 & 0 & 0 & 1 & 1 & 0 & 0 & 0 & 0 \\ 0 & 0 & 0 & 0 & 0 & J & 1 & 0 & 0 \\ 0 & 0 & 0 & 0 & 0 & 0 & 0 & 1 & J \end{bmatrix} \begin{Bmatrix} \partial W_1^p/\partial y_1 \\ \partial W_2^p/\partial y_2 \\ \partial W_3^p/\partial y_3 \\ \partial W_1^p/\partial y_2 \\ \partial W_2^p/\partial y_1 \\ \partial W_2^p/\partial y_3 \\ \partial W_3^p/\partial y_2 \\ \partial W_3^p/\partial y_1 \\ \partial W_1^p/\partial y_3 \end{Bmatrix} = \bar{\mathbf{B}}(\mathbf{y})^{\mathrm{n}} \mathbf{W}_e^p \tag{35}$$

Here $\bar{\mathbf{B}}(\mathbf{y})$ is also different from conventional strain-displacement matrix and is denoted with an overbar.

In Eq.(34), the element stiffness matrix $\mathbf{k}$ is formulated in the $Oy_1y_2y_3$ coordinate, and can be alternatively integrated in the $O\eta_1\eta_2\eta_3$ coordinate, given by

$$\mathbf{k}_e = \int_{\Omega_e'} \left[\mathbf{B}(\boldsymbol{\eta})\right]^{\mathrm{T}} \mathbf{c}\mathbf{B}(\boldsymbol{\eta}) |\mathbf{J}| d\boldsymbol{\eta} = J \int_{\Omega_e'} \left[\mathbf{B}(\boldsymbol{\eta})\right]^{\mathrm{T}} \mathbf{c}\mathbf{B}(\boldsymbol{\eta}) d\boldsymbol{\eta} = J\mathbf{k}_e^{\eta} \tag{36}$$

where Ω_e' is the domain of e-th element in the $O\eta_1\eta_2\eta_3$ coordinate, projected from Ω_e in the $Oy_1y_2y_3$ coordinate, $\mathbf{B}(\boldsymbol{\eta})$ is the conventional strain-displacement matrix, and $\mathbf{k}_e^{\eta}$ is the conventional stiffness matrix constructed in the $O\eta_1\eta_2\eta_3$ coordinate. Therefore, Eq.(36) is more convenient for element stiffness matrix formulation and structural analysis, as compared with Eq.(34). On the other hand, in the field of structural optimization, as the Jacobian coefficient J is explicitly manifested in the matrix $\bar{\mathbf{B}}$ in Eq.(34), analytical sensitivity analysis of stiffness $\mathbf{k}$ with respect to J is readily accessible. In Eq.(36), however, the Jacobian coefficient J is implicitly reflected in the nodal coordinates and sensitivity analysis cannot be directly acquired. Hence, Eq.(34) is more favorable from optimization point of view.

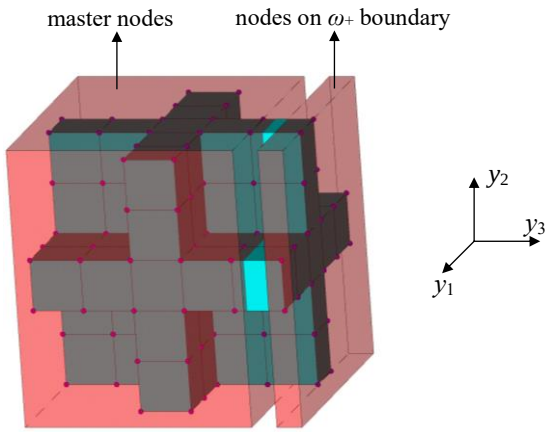

Figure 3. Sketch of the unit cell FE model (Red dots denote element nodes and master nodes are obtained by subtracting nodes on ω_+ boundary from full nodes in the unit cell.)

Denote by the global displacement vector ${}^{\mathrm{n}}\mathbf{W}^p = \mathop{\mathrm{A}}_{e=1}^{n_e} {}^{\mathrm{n}}\mathbf{W}_e^p$, where A is the assembly operator, and the independent DOFs are a subset of ${}^{\mathrm{n}}\mathbf{W}^p$ as the periodic boundary condition in Eq. should be secured. In this work, the independent DOFs are defined on master nodes, which are obtained by subtracting nodes on ω_+ boundary from all nodes of the FE model in Figure 3, and are denoted by ${}^{\mathrm{n}}\mathbf{W}_{\mathrm{m}}^p$ with a right subscript m. The relation between ${}^{\mathrm{n}}\mathbf{W}^p$ and ${}^{\mathrm{n}}\mathbf{W}_{\mathrm{m}}^p$ can be characterized by

$$ {}^{\mathrm{n}}\mathbf{W}^p = \mathbf{T}\,{}^{\mathrm{n}}\mathbf{W}_{\mathrm{m}}^p + \Delta\,{}^{\mathrm{n}}\mathbf{V}^p \tag{37} $$

where $\mathbf{T}$ is the transformation matrix [30], which transforms DOFs on master nodes to full DOFs. I practical applications, the matrix $\mathbf{T}$ is not explicitly assembled but fulfilled through row and column addition operation of matrices in the FE codes, as detailed in Appendix A. $\Delta\,{}^{\mathrm{n}}\mathbf{V}^p$ is the displacement vector constructed according to $\Delta\mathbf{V}^p$ in Eq.(28) , which has the length of full nodal degrees of freedom and has non-zeros values only on the ω_+ boundary. Substitute Eq.(37 into Eq.(33) and the solution formulation for displacement vector $\mathbf{W}^p$ is expressed as

$$ \begin{aligned} &\mathbf{T}^{\mathrm{T}}\mathbf{k}\mathbf{T}\,{}^{\mathrm{n}}\mathbf{W}_{\mathrm{m}}^p = -\mathbf{T}^{\mathrm{T}}\mathbf{F}^p, \mathbf{F}^p = \mathbf{k}\Delta\,{}^{\mathrm{n}}\mathbf{V}^p \\ &{}^{\mathrm{n}}\mathbf{W}^p = \mathbf{T}\,{}^{\mathrm{n}}\mathbf{W}_{\mathrm{m}}^p + \Delta\,{}^{\mathrm{n}}\mathbf{V}^p \end{aligned} \tag{38} $$

Here $\mathbf{k}$ is the global stiffness matrix $\mathbf{k} = \mathop{\mathrm{A}}_{e=1}^{n_e} \mathbf{k}_e$, and identical FE mesh on periodic boundaries $\omega_\pm$ is presumed for the applicability of transformation matrix $\mathbf{T}$. To resolve Eq.(38) , rigid body displacements, i.e., three rigid-body translations along y_1, y_2, y_3 axes and a rigid-body rotation around y axis, should be excluded. In the FE codes in Appendix A, the rigid-body translations are suppressed by constraining all translational displacement components of one node, and the rigid-body rotation is suppressed by constraining a proper displacement component of a surrounding node. Therefore, the remaining DOFs, that are acquired through subtracting DOFs suppressing rigid-body displacements from those on master nodes, are resolved through Eq.(38) Once the displacements $\mathbf{V}^p$ (=1, 2, 3, 4) are resolved, the effective stiffness can be calculated as

$$ D^{pq} = \frac{1}{|Y|}\left({}^{\mathrm{n}}\mathbf{W}^p\right)^{\mathrm{T}} \mathbf{k}\,{}^{\mathrm{n}}\mathbf{W}^q \tag{39} $$

where p, q=1,2,3,4.

4.2 Effective stiffness and unit cell problem formulation for shell elements

For unit cells composed of structures with contrast member sizes, the adoption of solid elements for FE discretization should involve large numbers of elements to acquire satisfactory results. To save computational resource and time without losing accuracy, the adoption of structural element types, such as shell elements, becomes indispensable. In this subsection, the unit cell problems for shell elements are derived.

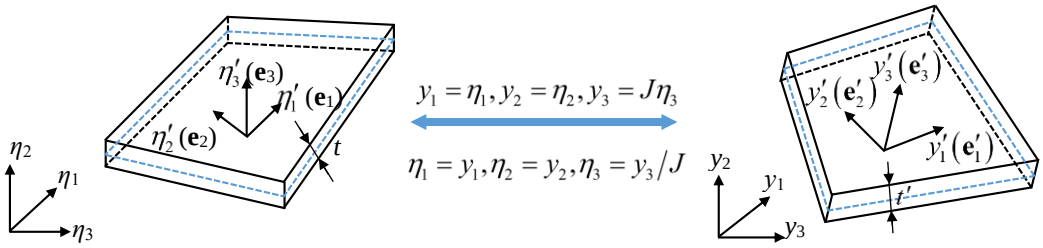

Figure 4. Sketch of the shell model in the $O\eta_1\eta_2\eta_3$ coordinate and its mapped shell model in the $Oy_1y_2y_3$ coordinate (Blue dashed lines represent mid-surfaces.)

First, consider a shell element of the unit cell in the $O\eta_1\eta_2\eta_3$ coordinate depicted in Figure 4, which is mapped into that of the unit cell in the $Oy_1y_2y_3$ coordinate. The shell local coordinates $O\eta_1'\eta_2'\eta_3'$ and $Oy_1'y_2'y_3'$ can be characterized by the unit orthonormal bases $\mathbf{e}_1$, $\mathbf{e}_2$, $\mathbf{e}_3$ and $\mathbf{e}_1'$, $\mathbf{e}_2'$, $\mathbf{e}_3'$ respectively. Here $\mathbf{e}_1$, $\mathbf{e}_2$ ($\mathbf{e}_1'$, $\mathbf{e}_2'$) lie within the mid-surface and $\mathbf{e}_3$ ($\mathbf{e}_3'$) is vertical to the mid-surface. The thicknesses are t and t' for shells in the $O\eta_1\eta_2\eta_3$ coordinate and those in the $Oy_1y_2y_3$ coordinate respectively. For solid elements, the stiffness matrix $\mathbf{k}$ can be constructed either in the $Oy_1y_2y_3$ coordinate through Eq.(34) or in the $O\eta_1\eta_2\eta_3$ coordinate through Eq.(36) depending on the problem encountered For shell element, where the strain-displacement relation is different from that of elastic continuum, the derivation of unconventional strain-displacement matrix $\bar{\mathbf{B}}(\mathbf{y})$ in Eq.(34) is much more complicated. To accommodate the unit cell problem formulation (38) to shell elements, the assembly of stiffness matrix $\mathbf{k}_e$ through Eq.(36) in the $O\eta_1\eta_2\eta_3$ coordinate is more favorable as different well developed shell elements can be utilized. In practical applications, if the unit cell model in the Oy_1y_2y coordinate, i.e., the vectors $\mathbf{e}_1'$, $\mathbf{e}_2'$, $\mathbf{e}_3'$ and the thickness t', is prior known, the unit orthonormal

vectors $\mathbf{e}_1$, $\mathbf{e}_2$, $\mathbf{e}_3$ and the thickness t in $O\eta_1\eta_2\eta_3$ coordinate can be constructed through the following relation

$$\mathbf{e}_1 = \frac{\mathbf{J}^{-1}\mathbf{e}_1'}{\left\|\mathbf{J}^{-1}\mathbf{e}_1'\right\|}, \mathbf{e}_3 = \frac{\left(\mathbf{J}^{-1}\mathbf{e}_1'\right)\times\left(\mathbf{J}^{-1}\mathbf{e}_2'\right)}{\left\|\left(\mathbf{J}^{-1}\mathbf{e}_1'\right)\times\left(\mathbf{J}^{-1}\mathbf{e}_2'\right)\right\|}, \mathbf{e}_2 = \mathbf{e}_3\times\mathbf{e}_1, t = \left(\mathbf{J}^{-1}\mathbf{e}_3'\right)\cdot\mathbf{e}_3 t' \tag{40}$$

Then the local element stiffness matrix $\mathbf{k}_e^{\text{local}}$ and the transformation matrix $\mathbf{T}_e$, which relates local and global coordinates, can be constructed for e-th element in the $O\eta_1\eta_2\eta_3$ coordinate. The global element stiffness matrix $\mathbf{k}_e^{\eta}$ is hence given by

$$\mathbf{k}_e^{\eta} = \mathbf{T}_e^{\mathrm{T}}\mathbf{k}_e^{\text{local}}\mathbf{T}_e \tag{41}$$

Alternatively, if the unit cell model in the $O\eta_1\eta_2\eta_3$ coordinate is acquired beforehand, then the stiffness matrix $\mathbf{k}_e^{\eta}$ can be directly constructed through Eq. With $\mathbf{k}_e^{\eta}$ in hand, the global stiffness matrix $\mathbf{k}$ is readily assembled through Eq. as $\mathbf{k} = J\overset{n_e}{\underset{e=1}{\mathrm{A}}}\mathbf{k}_e^{\eta}$.

To resolve the unit cell problem (38) for shell elements numerically, the displacement fields $\Delta\mathbf{V}^p = \mathbf{V}^p\big|_{\omega_+} - \mathbf{V}^p\big|_{\omega_-}$ in the periodic boundary condition should be transformed to include rotational DOFs in three steps. Firstly, the displacements $\mathbf{V}^p$ in Eq. is transformed into the local coordinate $O\eta_1'\eta_2'\eta_3'$ in Figure 4 as

$$\eta_i' = e_{ij}\eta_j, V_i'^p = e_{ij}V_j^p \tag{42}$$

where e_{ij} is the j-th component of vector $\mathbf{e}_i$, and $\mathbf{V}'^p$ is the displacement in local coordinate. Secondly, the rotational angles are calculated as

$$\begin{aligned}
\theta_1'^p &= -\frac{\partial V_2'^p}{\partial\eta_3'} = -e_{2j}e_{3i}\frac{\partial V_j^p}{\partial\eta_i}, \theta_2'^p = \frac{\partial V_1'^p}{\partial\eta_3'} = e_{1j}e_{3i}\frac{\partial V_j^p}{\partial\eta_i} \\
\theta_3'^p &= \frac{1}{2}\left(\frac{\partial V_2'^p}{\partial\eta_1'} - \frac{\partial V_1'^p}{\partial\eta_2'}\right) = \frac{1}{2}\left(e_{2j}e_{1i} - e_{1j}e_{2i}\right)\frac{\partial V_j^p}{\partial\eta_i}
\end{aligned} \tag{43}$$

Here the Allman-type drilling DOF $\theta_3'^p$ is adopted [50,51]. Thirdly, the rotational angles are transformed back into the global coordinate $O\eta_1\eta_2\eta_3$, given by

$$\theta_i^p = e_{ji}\theta_j'^p \tag{44}$$

Substituting Eq. into Eq.(42) and following the procedure in Eqs.(42 (44 , the analytical expressions for $\boldsymbol{\theta}^p$ can be acquired. Therefore, the periodic boundary condition for shell elements that includes both translational and rotational DOFs is characterized as

$$\begin{aligned}
&\Delta\mathbf{V}^p = \mathbf{V}^p\big|_{\omega_+} - \mathbf{V}^p\big|_{\omega_-}, \Delta\boldsymbol{\theta}^p = \boldsymbol{\theta}^p\big|_{\omega_+} - \boldsymbol{\theta}^p\big|_{\omega_-} \quad (p=1,2,3,4)\\
&\Delta\mathbf{V}^1 = \begin{Bmatrix} 0 \\ 0 \\ l/J \end{Bmatrix}, \Delta\mathbf{V}^2 = \begin{Bmatrix} 0 \\ 0 \\ ly_1/J \end{Bmatrix}, \Delta\mathbf{V}^3 = \begin{Bmatrix} 0 \\ 0 \\ ly_2/J \end{Bmatrix}, \Delta\mathbf{V}^4 = \begin{Bmatrix} -ly_2/J \\ ly_1/J \\ 0 \end{Bmatrix}\\
&\Delta\boldsymbol{\theta}^1 = \begin{Bmatrix} 0 \\ 0 \\ 0 \end{Bmatrix}, \Delta\boldsymbol{\theta}^2 = \Delta\begin{Bmatrix} 0 \\ -l/J \\ 0 \end{Bmatrix}, \Delta\boldsymbol{\theta}^3 = \begin{Bmatrix} l/J \\ 0 \\ 0 \end{Bmatrix}, \Delta\boldsymbol{\theta}^4 = \begin{Bmatrix} 0 \\ 0 \\ l/J \end{Bmatrix}
\end{aligned} \tag{45}$$

It is worth mentioning that, with the introduction of the Allman-type drilling DOF in Eq. $\Delta\boldsymbol{\theta}^p$ formulation only involves global nodal coordinate in Eq.(45) and element-wise parameters e_{ij} are all cancelled out. This significantly simplifies numerical implementation as elementwise rotational angle transformation is omitted. Another treatment is to simply let $\theta_3'^p = 0\left(p=1,2,3,4\right)$ and associate a small positive quantity with the drilling DOF to avoid element stiffness matrix singularity. In this case, direction cosines e_{ij} in local shell coordinates cannot be cancelled out in $\Delta\boldsymbol{\theta}^p$ and elementwise computation on periodic boundaries $\omega_\pm$ is inevitable, which could be quite tedious for complicated microstructures. The detailed derivation of $\Delta\boldsymbol{\theta}^p$ based on the above two treatments can be found in Appendix B.

With the stiffness matrix and displacement periodic boundary condition obtained for shell elements, the numerical formulation for unit cell problems are analogously constructed and resolved, and the effective stiffness can be calculated through Eq.

5. Numerical examples

In this section, four numerical examples, i.e., the zigzag beam, the sinus beam, the sandwich beam and the Schwartz-P beam, are presented to illustrate the correctness of the proposed method for both solid and shell elements. During the pre-processing stage, the geometrical models and FE meshes of the unit cells are created through the APDL code in ANSYS 17.1, the FE implementation of effective stiffness computation in Section 4 is conducted in MATLAB2018, and the FE analysis of the de-homogenized graded beams during the post-processing stage is again performed through the APDL code in ANSYS 17.1.

5.1 The zigzag beam example

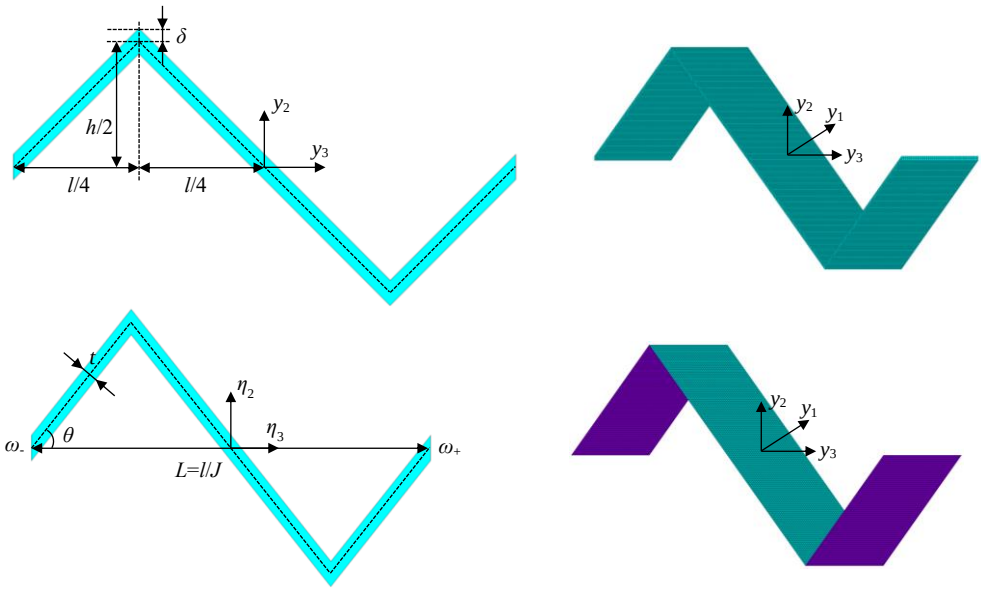

(a). Sizes of the zigzag beam in the $Oy_1y_2y_3$ and the $O\eta_1\eta_2\eta_3$ coordinates

(b). FE meshes of both solid and shell elements in the $Oy_1y_2y_3$ coordinate

Figure 5. Sketch and FE mesh of the zigzag beam unit cell

The first example is the zigzag-shaped beam in Figure 5(a), where the size parameters of the unit cell are defined in the $Oy_1y_2y_3$ coordinate with l=40, b=10, h=20, δ=0.2. The sizes of the deformed unit cell in the $O\eta_1\eta_2\eta_3$ coordinate are accordingly calculated with $L=l/J$, $\theta=\tan^{-1}(h/L)$, $t=2\delta\cos\theta$ in Figure 5(a). The material property is isotropic with Young's modulus E=2e5 and Poisson's ratio v=0.0.

The effective stiffness of the zigzag beam is first analyzed with solid elements, where the stiffness matrix is constructed through Eq. in the $Oy_1y_2y_3$ coordinate. Here the unit cell model in the $Oy_1y_2y_3$ coordinate is discretized with 45360 15-node tri-prism solid elements, depicted in Figure 5(b). The diagonal effective stiffness coefficients with different Jacobian coefficients J are listed in Table 1, where the off-diagonal terms are not listed as they are at least five orders of magnitude smaller. Homogenization of such corrugated beam structures has also been studied in [26], and the analytical results of $D^{11}_{\text{analytical}}$ and $D^{33}_{\text{analytical}}$ for the zigzag beam can be accordingly obtained. It is observed that the calculated analytical results, listed in Table 2, agree well with those in Table 1, and the largest relative error is 3.03% for J=2.0.

The effective stiffness is also calculated with shell elements, where the shell model is constructed and discretized in the $Oy_1y_2y_3$ coordinate in Figure 5(b). To formulate the stiffness matrix in the $O\eta_1\eta_2\eta_3$ coordinate, the local orthonormal basis and shell thickness are acquired through Eq.

matrix is assembled with 4-node Mindlin shell elements, where the enhanced assumed strain method is adopted to prevent shear locking [52].

The effective stiffness coefficients calculated with 2400 shell elements are listed in Table 3, where the relative errors compared to those obtained with solid elements are also listed in brackets. The results exhibit excellent agreement between solid and shell elements, showing the high precision of shell elements.

The calculation of effective stiffness is implemented on a laptop with an Intel core i7 8750H processor, 32GB memory and MATLAB 2018a. The computational time for shell and solid elements is around 0.6s and 15s respectively, showing the efficiency of shell elements. In addition, to propagate application of the proposed method, the implementation details for the zigzag beam composed of shell elements are presented in the 80-line MATLAB code in Appendix A.

Table 1. Stiffness coefficients of the zigzag beam obtained with solid elements

J	D^{11}	D^{22}	D^{33}	D^{44}
0.4	2.38e2	1.19e5	7.93e3	1.80e4
0.6	1.74e2	4.73e4	5.77e3	1.53e4
0.8	1.20e2	2.28e4	3.98e3	1.28e4
1.0	8.09e1	1.23e4	2.68e3	1.05e4
1.2	5.46e1	7.11e3	1.80e3	8.62e3
1.4	3.73e1	4.37e3	1.22e3	7.11e3
1.6	2.59e1	2.82e3	8.49e2	5.93e3
1.8	1.83e1	1.89e3	5.99e2	4.99e3
2.0	1.32e1	1.30e3	4.31e2	4.24e3

Table 2. Analytical stiffness coefficients of the zigzag beam

J	$D^{11}_{\text{analytical}}$	$D^{33}_{\text{analytical}}$
0.4	2.38e2 (0.00%)	7.93e3 (0.00%)
0.6	1.73e2 (-0.57%)	5.77e3 (0.00%)
0.8	1.19e2 (-0.83%)	3.97e3 (-0.25%)
1.0	8.00e1 (-1.11%)	2.67e3 (-0.37%)
1.2	5.37e1 (-1.65%)	1.79e3 (-0.56%)
1.4	3.65e1 (-2.14%)	1.22e3 (0.00%)
1.6	2.52e1 (-2.70%)	8.42e2 (-0.82%)

1.8	1.78e1 (-2.73%)	5.93e2 (-1.00%)
2.0	1.28e1 (-3.03%)	4.27e2 (-0.93%)

Table 3. Stiffness coefficients of the zigzag beam obtained with shell elements

J	D^{11}	D^{22}	D^{33}	D^{44}
0.4	2.38e2 (0.0%)	1.20e5 (0.84%)	7.93e3 (0.00%)	1.81e4 (0.56%)
0.6	1.73e2 (-0.57%)	4.76e4 (0.63%)	5.77e3 (0.00%)	1.55e4 (1.31%)
0.8	1.19e2 (-0.83%)	2.29e4 (0.44%)	3.97e3 (-0.25%)	1.28e4 (0.00%)
1.0	8.00e1 (-1.11%)	1.23e4 (0.00%)	2.67e3 (-0.37%)	1.05e4 (0.00%)
1.2	5.37e1 (-1.65%)	7.12e3 (0.14%)	1.79e3 (-0.56%)	8.65e3 (0.35%)
1.4	3.65e1 (-2.14%)	4.36e3 (-0.23%)	1.22e3 (0.00%)	7.13e3 (0.28%)
1.6	2.53e1 (-2.32%)	2.81e3 (-0.35%)	8.42e2 (-0.82%)	5.94e3 (0.17%)
1.8	1.78e1 (-2.73%)	1.87e3 (-1.06%)	5.93e2 (-1.00%)	4.99e3 (0.00%)
2.0	1.28e1 (-3.03%)	1.30e3 (0.00%)	4.27e2 (-0.93%)	4.23e3 (-0.24%)

5.2 The sinus beam example

The second example is the sinus beam in Figure 6. Different from the first example, the size parameters are defined in the $O\eta_1\eta_2\eta_3$ coordinate, where D=40, $L=l/J$, l=20, b=6, δ=0.4, and the unit cell is discretized with 15-node tri-prism solid elements. Hence, the stiffness matrix is directly assembled through Eq. in the $O\eta_1\eta_2\eta_3$ coordinate. The calculated effective stiffness coefficients with different Jacobian coefficients J are listed in Table 4, where the off-diagonal terms are not listed as they are at least five orders of magnitude smaller. On the other hand, the analytical results of effective stiffness $D^{11}_{\text{analytical}}$ and $D^{33}_{\text{analytical}}$ for the sinus beam can also be acquired following the method in [23].

The calculated analytical results are listed in Table 5. It is observed that the results in Tables 4 and 5 are in excellent agreement and the relative errors are all well below 1%, signifying the accuracy and effectiveness of the proposed method.

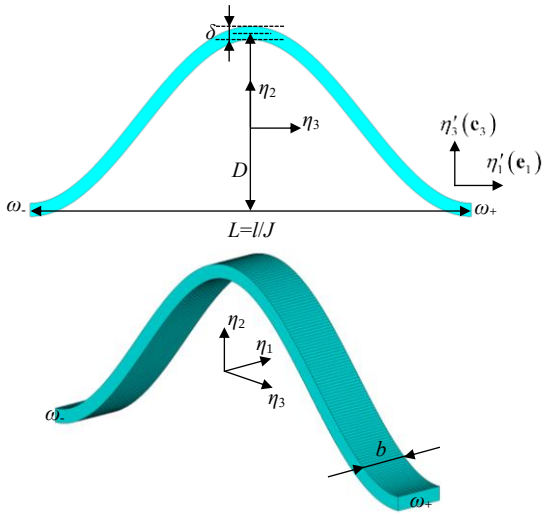

(a). Sizes of the sinus beam in $O\eta_1\eta_2\eta_3$ coordinate

(b). Shell model of the sinus beam

Figure 6. Sketch of the sinus beam unit cell

The shell model of the sinus beam is depicted in Figure 6(b), and the effective stiffness coefficients acquired with shell elements are listed in Table 6, where the relative errors compared to those obtained with solid elements are well below 1%, illustrating the high accuracy of shell elements. The computational time for the FE model composed of 37152 solid elements is around 10s and that of the FE model composed of 4000 shell elements is around 1.3s, which is much more efficient without losing accuracy.

Table 4. Effective stiffness coefficients calculated with solid elements for the sinus beam

J	D^{11}	D^{22}	D^{33}	D^{44}
0.4	1.09e2	2.27e4	4.85e3	1.57e4
0.6	9.55e1	1.31e4	3.95e3	1.85e4
0.8	8.31e1	9.25e3	3.28e3	2.14e4
1.0	7.30e1	7.19e3	2.78e3	2.43e4
1.2	6.46e1	5.91e3	2.40e3	2.72e4
1.4	5.77e1	5.02e3	2.10e3	3.00e4
1.6	5.20e1	4.37e3	1.87e3	3.27e4
1.8	4.73e1	3.88e3	1.68e3	3.53e4
2.0	4.32e1	3.48e3	1.53e3	3.78e4

Table 5. Analytical effective stiffness coefficients of the sinus beam

J	$D^{11}_{\text{analytical}}$	$D^{33}_{\text{analytical}}$
0.4	1.09e2 (0.00%)	4.85e3 (0.00%)

0.6	9.55e1 (0.00%)	3.95e3 (0.00%)
0.8	8.32e1 (0.12%)	3.28e3 (0.00%)
1.0	7.31e1 (0.14%)	2.78e3 (0.00%)
1.2	6.47e1 (0.15%)	2.40e3 (0.00%)
1.4	5.79e1 (0.35%)	2.10e3 (0.00%)
1.6	5.22e1 (0.38%)	1.87e3 (0.00%)
1.8	4.75e1 (0.42%)	1.68e3 (0.00%)
2.0	4.35e1 (0.69%)	1.53e3 (0.00%)

Table 6. Effective stiffness coefficients calculated with shell elements for the sinus beam

J	D^{11}	D^{22}	D^{33}	D^{44}
0.4	1.09e2 (0.00%)	2.27e4 (0.00%)	4.85e3 (0.00%)	1.57e4 (0.00%)
0.6	9.55e1 (0.00%)	1.31e4 (0.00%)	3.95e3 (0.00%)	1.85e4 (0.00%)
0.8	8.32e1 (0.12%)	9.28e3 (0.32%)	3.28e3 (0.00%)	2.14e4 (0.00%)
1.0	7.30e1 (0.00%)	7.21e3 (0.28%)	2.78e3 (0.00%)	2.41e4 (-0.82%)
1.2	6.47e1 (0.15%)	5.92e3 (0.17%)	2.40e3 (0.00%)	2.72e4 (0.00%)
1.4	5.78e1 (0.17%)	5.03e3 (0.20%)	2.10e3 (0.00%)	2.99e4 (-0.33%)
1.6	5.21e1 (0.19%)	4.38e3 (0.23%)	1.87e3 (0.00%)	3.26e4 (-0.31%)
1.8	4.75e1 (0.42%)	3.89e3 (0.26%)	1.68e3 (0.00%)	3.52e4 (-0.28%)
2.0	4.35e1 (0.69%)	3.49e3 (0.29%)	1.53e3 (0.00%)	3.76e4 (-0.53%)

5.3 The sandwich beam example

The third example is the sandwich beam whose unit cell in the $O\eta_1\eta_2\eta_3$ coordinate is depicted in Figure 7(a). Here the size parameters are l=0.375, h=0.5, and the thicknesses of the core and the face sheets are t_c=0.01 and t_p=0.005 respectively. The material property is isotropic with E=1, v=0.3. The unit cell is modeled with 4-node shell elements depicted in Figure 7(b). The implementation approach in Section 4 is conducted in MATLAB to acquire the effective stiffness coefficients, listed in Table 7, and the same implementation procedure is also carried out in ANSYS for comparison purpose. The relative errors are all within 2%, validating the correctness of the in-house MATLAB code.

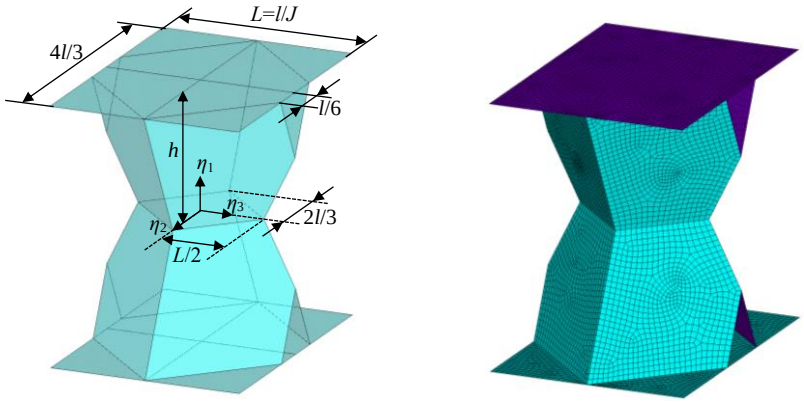

(a). Sizes of the sandwich beam unit cell (b). FE mesh of the sandwich beam unit cell

Figure 7. Sketch of the sandwich beam unit cell

Table 7. Effective stiffness coefficients for the sandwich beam example

J	D^{11}		D^{22}		D^{33}		D^{44}	
	MATLAB	ANSYS	MATLAB	ANSYS	MATLAB	ANSYS	MATLAB	ANSYS
1.0	5.39e-3	5.37e-3	3.23e-4	3.22e-4	1.08e-4	1.08e-4	5.84e-5	5.80e-5
0.5	6.56e-3	6.48e-3	3.76e-4	3.74e-4	1.24e-4	1.24e-4	6.27e-5	6.18e-5
2.0	5.11e-3	5.10e-3	3.15e-4	3.14e-4	1.05e-4	1.05e-4	4.64e-5	4.57e-5

In addition, the stiffness coefficients in Table 7 can also verified by beam deflections. Consider a periodic beam structure constructed by repeating the unit cell along the axial direction n times in Figure 8. The left side is clamped and the nodes on the right side are rigidly coupled with the center node. Four load cases in Figure 8(a) are applied on the center node, and the corresponding displacements u_{30}, u_{10}, u_{20}, θ_0 are respectively extracted from FE analysis. As n increases, the behavior of the beam gradually resembles the homogenized Euler-Bernoulli beam, and the effective stiffness can be estimated by the displacements at the tip end of the periodic beam. The analytical relations are expressed as follows

$$D'^{11}=\frac{N_0(nL)}{u_{30}}, D'^{22}=\frac{M_0(nL)^2}{2u_{10}}, D'^{33}=\frac{M_0(nL)^2}{2u_{20}}, D'^{44}=\frac{T_0(nL)}{\theta_0} \tag{46}$$

where $D'^{ii}\left(i=1,2,3,4\right)$ are the predicted effective stiffness coefficients.

Define the normalized stiffness as $\bar{D}^{ii}=\frac{D'^{ii}}{D^{ii}}\left(i=1,2,3,4\right)$, and the graphs of $\bar{D}^{ii}$ with respect to n are illustrated in Figure 9 for different values of J. As n increases, the extensional stiffness $\bar{D}^{11}$ and two bending stiffnesses $\bar{D}^{22},\bar{D}^{33}$ quickly converge at around n=20 and the rotational stiffness $\bar{D}^{44}$

gradually converges at n=45. The converged normalized stiffness coefficients all fall within the interval [1.00, 1.05], signifying small differences between D'^{ii} and D^{ii} (i=1,2,3,4). Therefore, the correctness of the stiffness coefficients in Table 7 is secured.

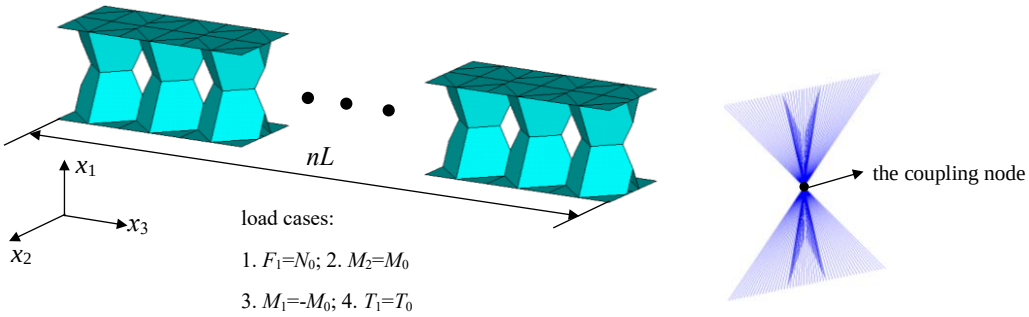

(a). The periodic beam structure

(b). Sketch of node rigid-coupling

Figure 8. Sketch of the periodic beam structure by repeating the unit cell n times

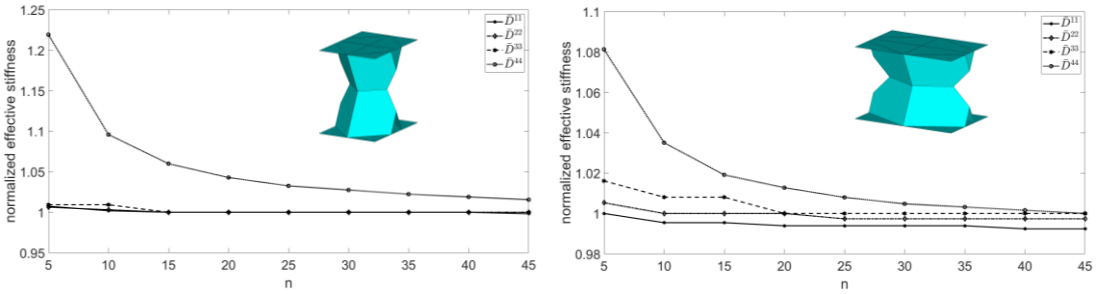

(a). Graph of normalized stiffness coefficients for J=1

(b). Graph of normalized stiffness coefficients for J=0.5

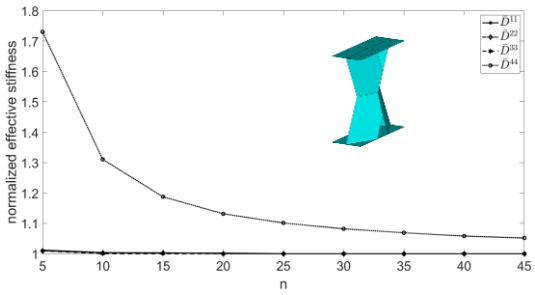

(c). Graph of normalized stiffness coefficients for J=2.0

Figure 9. Graph of normalized effective coefficients w.r.t. beam length for sandwich beam structures

Furthermore, consider a graded beam mapped from periodic ones, and the mapping functions are given as follows

$$\xi_3 = \begin{cases} Ax_3^3 + Bx_3^2 + Cx_3, (0 \le x_3 \le 18l) \\ D - A(36l - x_3)^3 - B(36l - x_3)^2 - C(36l - x_3), (18l \le x_3 \le 36l) \end{cases} \quad (47)$$
$$D = 2\left[A(18l)^3 + B(18l)^2 + 18Cl \right]$$

Here A=-0.02414, B=0.2667, C=0.5. The graph of the mapping function and the Jacobian coefficient J is depicted in Figure 10(a), and the graded beam is depicted in Figure 10(b). The left and right sides of the graded beam are clamped and a uniform pressure p=6.25×10^{-5} is applied on the top face sheet. Then the deflection contour is depicted in Figure 10(c). On the other hand, with the Jacobian coefficient J in Figure 10(a), the homogenized beam with graded effective stiffness can be constructed and the deflection contour is accordingly illustrated in Figure 10(d). It is observed that the two agree well with each other and the relative error of maximum deflection is merely 3.4%, illustrating the correctness of the proposed homogenization approach.

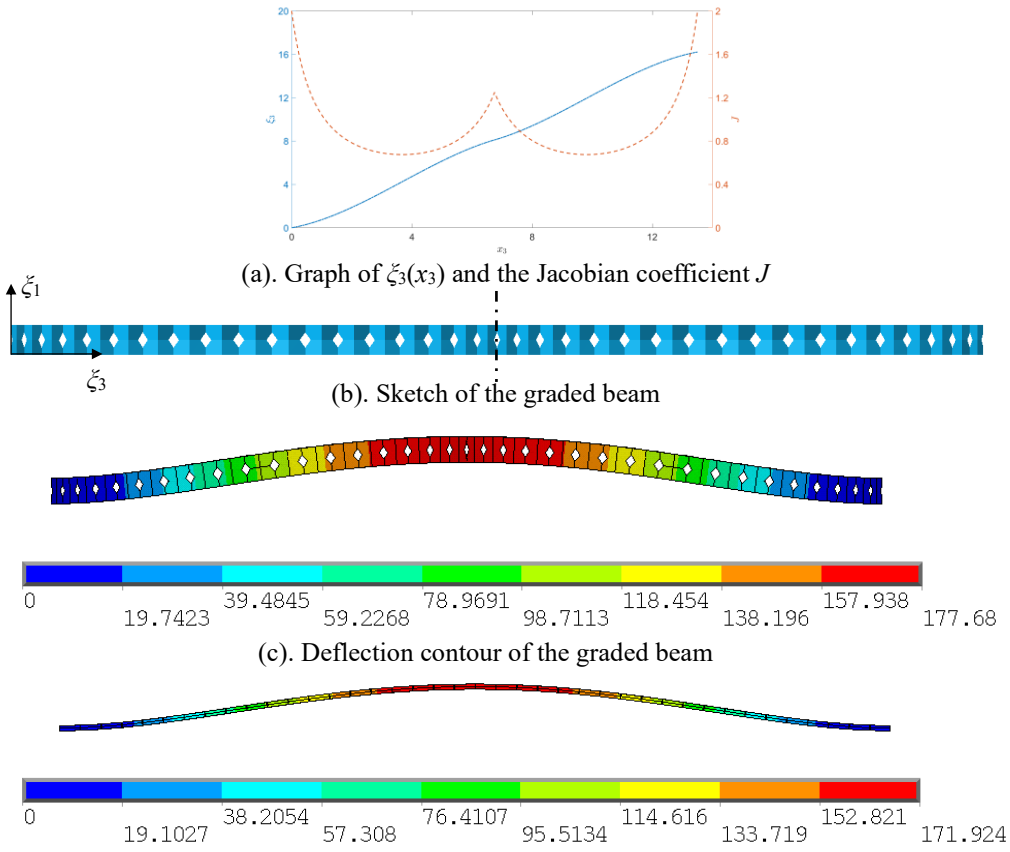

(a). Graph of $\xi_3(x_3)$ and the Jacobian coefficient J

(b). Sketch of the graded beam

(c). Deflection contour of the graded beam

(d). Deflection contour of the homogenized beam

Figure 10. Sketch and deflection contours of the graded sandwich beam

5.4 The Schwartz-P surface beam example

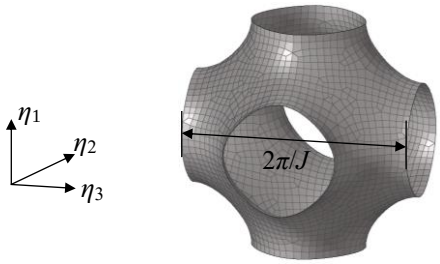

Figure 11. Mesh of the Schwartz-P surface unit cell

The last example is the beam whose unit cell is the Schwartz-P surface in the $Oy_1y_2y_3$ coordinate, and therefore the surface in the $O\eta_1\eta_2\eta_3$ coordinate is defined as $\cos\eta_1+\cos\eta_2+\cos J\eta_3=0$, as depicted in Figure 11. The thickness is t=0.02, and the material property is isotropic with E=1, v=0.3. The effective stiffness coefficients obtained through the in-house MATLAB code and the commercial software ANSYS are obtained in Table 8, where the relative errors are all within 2%.

Besides, the same procedure in subsection 5.3 is also carried out to verify the stiffness coefficients through beam deflections, the normalized stiffness coefficients w.r.t. beam length are depicted in Figure 12. Here the converged normalized stiffness coefficients are all within the range [1.00, 1.03], again showing the correctness of the proposed method.

Table 8. Effective stiffness coefficients for the Schwartz-P beam example

J	D^{11}		D^{22}		D^{33}		D^{44}	
	MATLAB	ANSYS	MATLAB	ANSYS	MATLAB	ANSYS	MATLAB	ANSYS
1.0	1.52e-4	1.53e-4	5.84e-4	5.89e-4	5.84e-4	5.89e-4	1.01e-2	1.02e-4
0.5	5.21e-4	5.24e-4	1.93e-3	1.96e-3	1.93e-3	1.96e-3	1.04e-2	1.05e-2
2.0	6.11e-5	6.13e-5	2.45e-4	2.48e-4	2.45e-4	2.48e-4	1.44e-2	1.46e-2

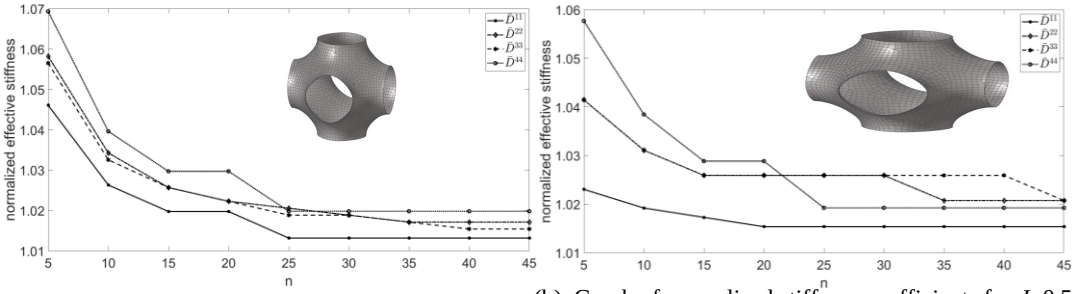

(a). Graph of normalized stiffness coefficients for J=1 (b). Graph of normalized stiffness coefficients for J=0.5

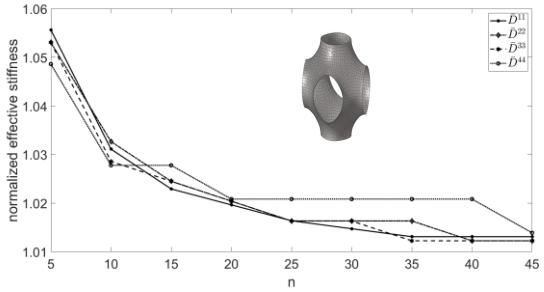

(c). Graph of normalized stiffness coefficients for J=2.0

Figure 12. Graph of normalized effective coefficients w.r.t. beam length for the Schwartz-P beam structure

Next we consider a graded Schwartz-P beam structure in Figure 13(b), which is mapped through the mapping function in Eq.

$$\xi_3 = \begin{cases} -A(18.5l - x_3)^3 - B(18.5l - x_3)^2 - C(18.5l - x_3) + D, (0 \le x_3 \le 18.5l) \\ A(x_3 - 18.5l)^3 + B(x_3 - 18.5l)^2 + C(x_3 - 18.5l) + D, (18.5l \le x_3 \le 37l) \end{cases} \tag{48}$$
$$D = A(18.5l)^3 + B(18.5l)^2 + 18.5Cl$$

Here A=-8.1412e-5, B=1.5485e-2, C=0.5. The graph of the mapping function and the Jacobian coefficient J is depicted in Figure 13(a). The left side of the beam is clamped and a concentrated force f=1×10^{-10} along x_1 direction is applied on the right hand side. Then the deflection contour is depicted in Figure 13(c), and that of the homogenized beam is illustrated in Figure 13(d). The relative error of maximum deflection is merely 1.7%, showing the effectiveness of the homogenization approach.

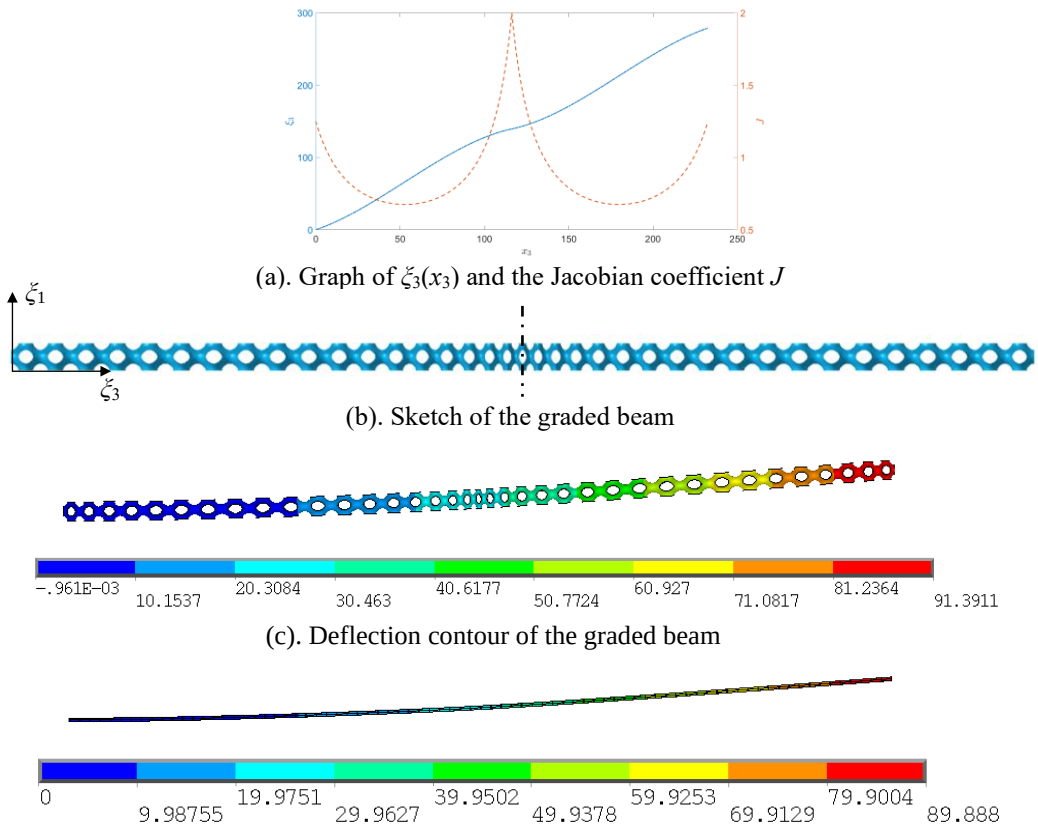

(a). Graph of $\xi_3(x_3)$ and the Jacobian coefficient J

(b). Sketch of the graded beam

(c). Deflection contour of the graded beam

(d). Deflection contour of the homogenized beam

Figure 13. Sketch and deflection contours of the graded Schwartz-P beam

6. Conclusions and comments

In this work, a novel numerical computational approach of effective stiffness is presented for spatially graded beam structures that are mapped from periodic ones. The numerical formulation for unit cell problems is first constructed and resolved for solid elements, where the introduction of Jacobian coefficients makes it different from conventional periodic beams. Then with the adoption of the Allman-type drilling DOF, the rotational DOFs in the periodic boundary condition can be derived into a unified formulation, where only global nodal coordinates are involved and tedious element-wise transformation of rotational angles is avoided. Hence, the unit cell problems for shell-structured microstructures and the corresponding numerical formulation are established in a concise form. Four numerical examples show the correctness of the proposed method in terms of both effective stiffness coefficients and beam deflection contours. Besides, with the adoption of shell elements, the computational efficiency is significantly improved without losing accuracy, as compared with that of solid elements. The presented

80-line MATLAB code illustrates the details of numerical implementation, and facilitates broadening application range of the proposed method.

With the above computation scheme, sensitivity analysis of effective stiffness is readily available, which paves the way for design optimization of spatially graded beams. Structural optimization of graded beams will be conducted in our future work.

Appendix A. An 80-line MATLAB code of effective stiffness calculation for the zigzag beam composed of shell elements

In Appendix A, the 80-line MATLAB code of effective stiffness calculation, which is presented in the supplementary material, is explained in detail for the unit cell composed of shell elements in subsection 5.1. This code serves as an introductory example for interested readers and as a basis for further improvements. It comprises two parts, i.e., the main routine and the subroutine. The main routine includes FE mesh information, global stiffness matrix assembly, displacement periodic boundary formulation and unit cell problem solution, and the subroutine is to construct element stiffness matrix.

The main routine is defined in lines 01-42. The basic size and material parameters of the unit cell are defined in line 02. Here b, h, l and deth respectively correspond to the dimensions b, h, l, δ of the unit cell in the $Oy_1y_2y_3$ coordinate in Figure 5(a). J0 is the gradient of the mapping function. theta and th respectively correspond to the dimensions θ and t of the unit cell in the $O\eta_1\eta_2\eta_3$ coordinate. E and v are the Young's modulus and Possion's ratio of the material respectively. The 3×3 matrix J and invJ denote the Jacobian matrix and its inverse.

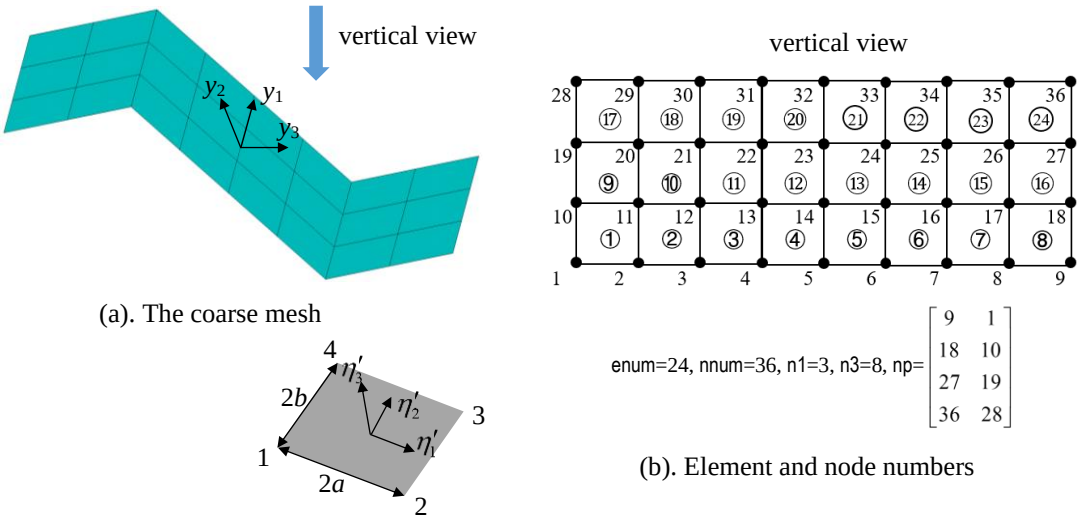

(a). The coarse mesh

(b). Element and node numbers

(c). Element node numbers in the local coordinate

Figure 14. An illustrative coarse mesh of the zigzag beam unit cell

The unit cell in the $Oy_1y_2y_3$ coordinate is assumed to be meshed with rectangular shell elements, where the element and node information of a coarse mesh is sketched in Figure 14. The mesh information is defined in lines 04-21. n1 and n3 denote the number of elements along y_1 and y_3 axes respectively, and nnum and enum stores the number of nodes and elements in the FE model respectively. Each element consists of 4 nodes with 6 DOFs per node. Both nodes and elements are numbered column-wise from left to right. The DOFs numbered from $6n$-5 to $6n$ correspond to three translational displacements and three rotational angles of node n. The enum×4 matrix enode and enum×24 matrix edof store the elemental node numbers and elemental DOF numbers respectively, where the i-th row contains the node numbers and DOF numbers of i-th element with i varying from 1 to enum. The nnum×3 matrix y contains the node coordinates in the $Oy_1y_2y_3$ coordinate and the nnum×3 matrix yita contains those in the $O\eta_1\eta_2\eta_3$ coordinate. The (n1+1)×2 matrix np stores paired node numbers on periodic boundaries ω_+ and ω_-, where the first column stores node numbers on ω_+ and second stores those on ω_-. The 6(n1+1)×2 matrix npdof contains the DOFs of the nodes in np. In FE solution of unit cell problems, not only the displacement periodic boundary condition should be imposed, but also the rigid-body displacements should be suppressed. In this code, the three translational DOFs of node 1 and the translational DOF along y_2 axis of node n3+2 is constrained to suppress rigid-body displacements. Therefore, the independent DOFs in unit cell problem

formulation, which is stored in the vector mdof, should be the full DOFs excluding DOFs on ω_+ boundary and DOFs for rigid body displacement suppression.

The assembly of global stiffness matrix is defined in lines 23-31. The vectors e1, e2 and e3 denote unit orthonormal basis vectors in the elemental local coordinate $O\eta_1'\eta_2'\eta_3'$. a and b are half the dimensions of the element along e1 and e2 respectively. The 24×24 matrix ke_local denotes the 4-node element stiffness matrix in local coordinates, the 24×24 matrix T denotes transformation matrix between local and global coordinates and the cell array ke is adopted to store all the element stiffness matrices in the global coordinate $O\eta_1\eta_2\eta_3$. The global stiffness matrix K is efficiently constructed by the sparse function, where the row and column index of the non-zero entries are stored in vectors iK and jK respectively.

The formulation of $\Delta\mathbf{V}^p$ and $\Delta\boldsymbol{\theta}^p$ in Eq.(45) is expressed by the 6nnum×24 matrix detW defined in lines 33-37, which only has non-zero entries on nodes on the ω_+ boundary. The unit cell problem and effective stiffness are resolved in lines 39-42. The matrix Fs corresponds to the term $-\mathbf{T}^{\mathrm{T}}\left[\mathbf{F}^1 \quad \mathbf{F}^2 \quad \mathbf{F}^3 \quad \mathbf{F}^4\right]$ and the matrix Ks corresponds to the term $\mathbf{T}^{\mathrm{T}}\mathbf{K}\mathbf{T}$ in Eq. numerical implementation, pre-multiplying $\mathbf{T}^{\mathrm{T}}$ is equivalent to row addition operation and post-multiplying $\mathbf{T}$ is equivalent to column addition operation. Therefore the transformation matrix $\mathbf{T}$ in Eq. is not assembled in the presented code. The 6nnum×24 matrix W is the displacement solution of the unit cell problem with p-th column corresponding to the displacement $\mathbf{W}^p$ in Eq. The 4×4 matrix DH is the effective stiffness matrix.

The subroutine ke_matrix.m calculating element stiffness matrix of the 4-node rectangular Mindlin shell element is defined in lines 43-80. The input parameters include half the dimensions of the element a and b, the thickness of the element th and material properties E and v. The output is the element stiffness matrix Ke. Here the matrix Km and Kb denote the membrane and bending part of the stiffness matrix. To prevent shear locking, the enhanced assumed strain method is adopted and the matrix Ks denotes the shear part of the stiffness matrix. In addition, the penalty term relating the drilling DOF to prevent numerical instability is applied as the matrix Kt. At last, the element stiffness Ke is constructed by adding the above four matrices.

The adopted mesh for effective stiffness calculation in Section 4.1 is n1=20, n3=120, and the mesh convergence analysis is conducted in Table 9 for J=1, where satisfactory results are acquired with n1=10, n3=60. Therefore the adopted mesh settings can acquire satisfactory results with high accuracy.

Table 9. Mesh convergence analysis for effective stiffness

n1	n3	D^{11}	D^{22}	D^{33}	D^{44}
5	30	8.58e1	1.29e4	2.72e3	1.04e4
10	60	8.01e1	1.23e4	2.67e3	1.06e4
20	120	8.00e1	1.23e4	2.67e3	1.05e4
40	240	8.00e1	1.22e4	2.67e3	1.05e4

Appendix B. Derivation of rotational DOFs in the periodic boundary condition

In appendix B, the derivation of $\Delta\boldsymbol{\theta}^p\left(p=1,2,3,4\right)$ are detailed. Firstly, the rotational DOFs $\boldsymbol{\theta}$ (p=1,2,3,4), which correspond to displacements $\mathbf{V}^p$ (p=1,2,3,4), can be acquired in matrix form according to Eqs

$$\boldsymbol{\theta}^1=\begin{Bmatrix} e_{33}\left(-e_{11}e_{23}+e_{21}e_{13}\right)\\ e_{33}\left(-e_{12}e_{23}+e_{22}e_{13}\right)\\ 0\end{Bmatrix},\boldsymbol{\theta}^2=\begin{Bmatrix} e_{33}\left(-e_{11}e_{23}+e_{21}e_{13}\right)\eta_1\\ \left[e_{31}\left(-e_{12}e_{23}+e_{22}e_{13}\right)+e_{33}\left(e_{12}e_{21}-e_{11}e_{22}\right)+e_{32}\left(e_{23}e_{11}-e_{21}e_{13}\right)\right]\eta_3+e_{33}\left(-e_{12}e_{23}+e_{22}e_{13}\right)\eta_1\\ 0\end{Bmatrix}$$

$$\boldsymbol{\theta}^3=\begin{Bmatrix} \left[e_{32}\left(-e_{11}e_{23}+e_{21}e_{13}\right)+e_{33}\left(e_{11}e_{22}-e_{12}e_{21}\right)+e_{31}\left(e_{23}e_{12}-e_{22}e_{13}\right)\right]\eta_3+e_{33}\left(-e_{11}e_{23}+e_{21}e_{13}\right)\eta_2\\ e_{33}\left(-e_{12}e_{23}+e_{22}e_{13}\right)\eta_2\\ 0\end{Bmatrix}$$

$$\boldsymbol{\theta}^4=\begin{Bmatrix} \eta_2\left(e_{11}e_{23}-e_{21}e_{13}\right)e_{31}/2+\eta_1e_{33}\left(-e_{11}e_{22}+e_{12}e_{21}\right)+\eta_1e_{31}\left(-e_{23}e_{12}+e_{22}e_{13}\right)/2\\ \eta_2e_{33}\left(e_{12}e_{21}-e_{11}e_{22}\right)+\eta_2e_{32}\left(e_{11}e_{23}-e_{21}e_{13}\right)/2+\eta_1e_{32}\left(-e_{23}e_{12}+e_{22}e_{13}\right)/2\\ \left[\left(e_{13}e_{21}-e_{23}e_{11}\right)e_{32}+\left(-e_{13}e_{22}+e_{23}e_{12}\right)e_{31}+\left(e_{11}e_{22}-e_{12}e_{21}\right)e_{33}\right]\eta_3+\eta_2e_{33}\left(e_{13}e_{21}-e_{23}e_{11}\right)/2+\eta_1e_{33}\left(-e_{13}e_{22}+e_{23}e_{12}\right)/2\end{Bmatrix}$$

(49)

Besides, as vectors $\mathbf{e}_1$, $\mathbf{e}_2$, $\mathbf{e}_3$ in local shell coordinate constitute unit orthogonal base vectors, the equalities $\mathbf{e}_1\times\mathbf{e}_2=\mathbf{e}_3,\left\|\mathbf{e}_3\right\|_2=1$ should hold. Cast in component form, they are rewritten as

$$e_{31}=e_{12}e_{23}-e_{13}e_{22},e_{32}=e_{13}e_{21}-e_{11}e_{23},e_{33}=e_{11}e_{22}-e_{12}e_{21},e_{31}^2+e_{32}^2+e_{33}^2=1 \quad (50$$

Substitute Eq.(50 into Eq.(49 , we acquire

$$\boldsymbol{\theta}^1=\begin{Bmatrix} e_{33}e_{32}\\ -e_{33}e_{31}\\ 0\end{Bmatrix},\boldsymbol{\theta}^2=\begin{Bmatrix} e_{33}e_{32}\eta_1\\ -\eta_3-e_{33}e_{31}\eta_1\\ 0\end{Bmatrix},\boldsymbol{\theta}^3=\begin{Bmatrix} \eta_3+e_{33}e_{32}\eta_2\\ -e_{33}e_{31}\eta_2\\ 0\end{Bmatrix},\boldsymbol{\theta}^4=\begin{Bmatrix} -\frac{1}{2}e_{31}e_{32}\eta_2-\eta_1e_{33}^2-\frac{1}{2}\eta_1e_{31}^2\\ -\frac{1}{2}\eta_1e_{32}e_{31}-\eta_2e_{33}^2-\frac{1}{2}\eta_2e_{32}^2\\ \eta_3+\frac{1}{2}\eta_2e_{33}e_{32}+\frac{1}{2}\eta_1e_{33}e_{31}\end{Bmatrix} \quad (51$$

In addition, as the shell structures are usually smoothly varying on the periodic boundaries, the surface normal also vary smoothly on periodic boundaries, which imply

$$e_{31}\big|_{\omega_+}=e_{31}\big|_{\omega_-},e_{32}\big|_{\omega_+}=e_{32}\big|_{\omega_-},e_{33}\big|_{\omega_+}=e_{33}\big|_{\omega_-} \quad (52$$

Therefore, $\Delta\boldsymbol{\theta}^p\left(p=1,2,3,4\right)$ can be stated as

$$\Delta\boldsymbol{\theta}^1=\begin{Bmatrix}0\\0\\0\end{Bmatrix},\Delta\boldsymbol{\theta}^2=\begin{Bmatrix}0\\-l/J\\0\end{Bmatrix},\Delta\boldsymbol{\theta}^3=\begin{Bmatrix}l/J\\0\\0\end{Bmatrix},\Delta\boldsymbol{\theta}^4=\begin{Bmatrix}0\\0\\l/J\end{Bmatrix}$$

The rotational DOF periodic boundary condition in Eq.

On the other hand, if we simply let $\theta_3'^p=0\left(p=1,2,3,4\right)$ in Eq.

DOF in the global coordinate can be calculated as

$$\boldsymbol{\theta}^1=\begin{Bmatrix}e_{33}\left(-e_{11}e_{23}+e_{21}e_{13}\right)\\e_{33}\left(-e_{12}e_{23}+e_{22}e_{13}\right)\\0\end{Bmatrix},\boldsymbol{\theta}^2=\begin{Bmatrix}e_{31}\left(-e_{11}e_{23}+e_{21}e_{13}\right)\eta_3+e_{33}\left(e_{21}e_{13}-e_{11}e_{23}\right)\eta_1\\\left[e_{31}\left(-e_{12}e_{23}+e_{22}e_{13}\right)+e_{33}\left(e_{12}e_{21}-e_{11}e_{22}\right)\right]\eta_3+e_{33}\left(-e_{12}e_{23}+e_{22}e_{13}\right)\eta_1\\e_{33}\left(e_{13}e_{21}-e_{23}e_{11}\right)\eta_3\end{Bmatrix}$$

$$\boldsymbol{\theta}^3=\begin{Bmatrix}\left[e_{32}\left(-e_{11}e_{23}+e_{21}e_{13}\right)+e_{33}\left(e_{11}e_{22}-e_{12}e_{21}\right)\right]\eta_3+e_{33}\left(-e_{11}e_{23}+e_{21}e_{13}\right)\eta_2\\e_{32}\left(-e_{12}e_{23}+e_{22}e_{13}\right)\eta_3+e_{33}\left(-e_{12}e_{23}+e_{22}e_{13}\right)\eta_2\\e_{33}\left(-e_{23}e_{12}+e_{13}e_{22}\right)\eta_3\end{Bmatrix}$$

$$\boldsymbol{\theta}^4=\begin{Bmatrix}e_{31}\left(-e_{11}e_{22}+e_{12}e_{21}\right)\eta_3+e_{33}\left(-e_{11}e_{22}+e_{12}e_{21}\right)\eta_1\\e_{32}\left(e_{12}e_{21}-e_{11}e_{22}\right)\eta_3+e_{33}\left(e_{12}e_{21}-e_{11}e_{22}\right)\eta_2\\\left[e_{31}\left(-e_{13}e_{22}+e_{23}e_{12}\right)+e_{32}\left(e_{13}e_{21}-e_{23}e_{11}\right)\right]\eta_3+e_{33}\left(e_{13}e_{21}-e_{23}e_{11}\right)\eta_2+e_{33}\left(-e_{13}e_{22}+e_{23}e_{12}\right)\eta_1\end{Bmatrix}$$

Substituting Eq.

$$\boldsymbol{\theta}^1=\begin{Bmatrix}e_{33}e_{32}\\-e_{33}e_{31}\\0\end{Bmatrix},\boldsymbol{\theta}^2=\begin{Bmatrix}e_{31}e_{32}\eta_3+e_{33}e_{32}\eta_1\\-\left(e_{31}^2+e_{33}^2\right)\eta_3-e_{33}e_{31}\eta_1\\e_{33}e_{32}\eta_3\end{Bmatrix},\boldsymbol{\theta}^3=\begin{Bmatrix}\left(e_{32}^2+e_{33}^2\right)\eta_3+e_{33}e_{32}\eta_2\\-e_{32}e_{31}\eta_3-e_{33}e_{31}\eta_2\\-e_{33}e_{31}\eta_3\end{Bmatrix}$$

$$\boldsymbol{\theta}^4=\begin{Bmatrix}-e_{33}e_{31}\eta_3-e_{33}^2\eta_1\\-e_{33}e_{32}\eta_3-e_{33}^2\eta_2\\\left(e_{31}^2+e_{32}^2\right)\eta_3+e_{33}e_{32}\eta_2+e_{33}e_{31}\eta_1\end{Bmatrix}$$

Considering Eq. $\Delta\boldsymbol{\theta}^p\left(p=1,2,3,4\right)$ is derived as

$$\Delta\boldsymbol{\theta}^1=\begin{Bmatrix}0\\0\\0\end{Bmatrix},\Delta\boldsymbol{\theta}^2=\begin{Bmatrix}e_{31}e_{32}y_3/J\\-\left(e_{31}^2+e_{33}^2\right)y_3/J\\e_{33}e_{32}\,y_3/J\end{Bmatrix},\Delta\boldsymbol{\theta}^3=\begin{Bmatrix}\left(e_{32}^2+e_{33}^2\right)y_3/J\\-e_{32}e_{31}\,y_3/J\\-e_{33}e_{31}\,y_3/J\end{Bmatrix},\Delta\boldsymbol{\theta}^4=\begin{Bmatrix}-e_{33}e_{31}\,y_3/J\\-e_{33}e_{32}\,y_3/J\\\left(e_{31}^2+e_{32}^2\right)y_3/J\end{Bmatrix}$$

Here the coefficients e_{ij} cannot be cancelled out in the periodic boundary condition and pointwise computation of surface normal on the periodic boundary is inevitable in Eq.

Data availability statement

The raw/processed data required to reproduce these findings cannot be shared at this time as the data also forms part of an ongoing study.

Funding

This work is supported by National Natural Science Foundation of China (No. 12002159), Natural Science Foundation of Jiangsu Province (No. BK20200411), the State Key Laboratory of Structural Analysis for Industrial Equipment (No. GZ20101), and a Project Funded by the Priority Academic Program Development of Jiangsu Higher Education Institutions (PAPD).

References

[1]. T. DebRoy, H. L. Wei, J. S. Zuback, T. Mukherjee, J. Elmer, J. O. Milewski, A. M. Beese, A. Wilson-Heid, A. De, W. Zhang. Additive manufacturing of metallic components–process, structure and properties. Prog. Mater. Sci., vol. 92, pp. 112-224, 2018.

[2]. Y. Liu, G. Zheng, N. Letov, Y. F. Zhao. A survey of modeling and optimization methods for multi-scale heterogeneous lattice structures. J. Mech. Design., vol. 143, no. 4, pp. 040803, 2021.

[3]. C. J. Ejeh, I. Barsoum, R. K. A. Al-Rub. Flexural properties of functionally graded additively manufactured AlSi10Mg TPMS latticed-beams. Int. J. Mech. Sci., vol. 223, pp. 107293, 2022.

[4]. A. Garg, H. D. Chalak, A. M. Zenkour, M. O. Belarbi, R. Sahoo. Bending and free vibration analysis of symmetric and unsymmetric functionally graded CNT reinforced sandwich beams containing softcore. Thin. Wall. Struct., vol. 170, pp. 108626, 2022.

[5]. M. O. Belarbi, M. S. A. Houari, H. Hirane, A. A. Daikh, S. P. A. Bordas. On the finite element analysis of functionally graded sandwich curved beams via a new refined higher order shear deformation theory. Compos. Struct., vol. 279, pp. 114715, 2022.

[6]. D. Cao, Y. Gao, M. Yao, W. Zhang. Free vibration of axially functionally graded beams using the asymptotic development method. Eng. Struct., vol. 173, pp. 442-448, 2018.

[7]. C. D. Chen, P. W. Su. An analytical solution for vibration in a functionally graded sandwich beam by using the refined zigzag theory. Acta. Mech., vol. 232, no. 11, pp. 4645-4668, 2021.

[8]. S. Zhao, Y. Zhang, Y. Zhang, J. Yang, Kitipornchai S. A functionally graded auxetic metamaterial beam with tunable nonlinear free vibration characteristics via graphene origami. Thin. Wall. Struct., vol. 181, pp. 109997, 2022.

[9]. D. Chen, S. Rezaei, P. L. Rosendahl, B. X. Xu, J. Schneider. Multiscale modelling of functionally graded porous beams: Buckling and vibration analyses. Eng. Struct., vol. 266, pp. 114568, 2022.

[10]. S. Zhao, Y. Zhang, H. Wu, Y. Zhang, J. Yang. Functionally graded graphene origami-enabled auxetic metamaterial beams with tunable buckling and postbuckling resistance. Eng. Struct., vol. 268, pp. 114763, 2022.

[11]. E. Carrera, M. Cinefra, M. Petrolo, E. Zappino. Finite element analysis of structures through unified formulation. John Wiley & Sons; 2014.

[12]. E. Carrera, I. Kaleel, M. Petrolo. Elastoplastic analysis of compact and thin-walled structures using classical and refined beam finite element models. Mech. Adv. Mater. Struct., vol. 26, pp. 274-286, 2019.

[13]. A. Pagani, E. Carrera. Unified formulation of geometrically nonlinear refined beam theories. Mech. Adv. Mater. Struct., vol. 25, pp. 15–31, 2018.

[14]. G. C. Tsiatas, A. E. Charalampakis. Optimizing the natural frequencies of axially functionally graded beams and arches. Compos. Struct., vol. 160, pp. 256-266, 2017.

[15]. I. V. Andrianov, J. Awrejcewicz, A.A. Diskovsky. Design optimization of FGM beam in stability problem. Eng. Computation., vol. 36, pp. 248-270, 2018.

[16]. A. S. Sayyad, Y. M. Ghugal. Modeling and analysis of functionally graded sandwich beams: A review. Mech. Adv. Mater. Struc., vol. 26, no. 21, pp. 1776-1795, 2019.

[17]. M. H. Ghayesh, A. Farajpour. A review on the mechanics of functionally graded nanoscale and microscale structures. Int. J. Eng. Sci., vol. 137, pp. 8-36, 2019.

[18]. A. Bensoussan, J. L. Lions, G. Papanicolaou. Asymptotic Analysis for Periodic Structures. Amsterdam: North Holland Publ, 1978.

[19]. A. L. Kalamkarov. Analysis, Design, and Optimization of Composite Structures. Chichester, New-York: John Wiley & Sons; 1997.

[20]. I. V. Andrianov, V. V. Danishevskyy, A. L. Kalamkarov. Asymptotic analysis of perforated plates and membranes. Part 1: Static problems for small holes. Int. J. Solids. Struct., vol. 49, no. 2, pp. 298-310, 2012.

[21]. A. G. Kolpakov, A. L. Kalamkarov. Homogenized thermoelastic model for a beam of a periodic structure. Int. J. Eng. Sci., vol. 37, no. 5, pp. 631-642, 1999.

[22]. A. G. Kolpakov. Stressed Composite Structures: Homogenized Models for Thin-walled Non-homogeneous Structures with Initial Stresses. Berlin, New-York: Springer-Verlag; 2004.

[23]. A. G. Kolpakov. The governing equations of a thin elastic stressed beam with a periodic structure. PMM-J. Appl. Math. Mec., vol. 63, no.3, pp. 495-504, 1999.

[24]. K. S. Challagulla, A. V. Georgiades, G. C. Saha, A. L. Kalamkarov. Micromechanical analysis of grid-reinforced thin composite generally orthotropic shells. Compos. Part B-eng., vol. 39, no. 4, pp. 627-644, 2008.

[25]. G. C. Saha, A. L. Kalamkarov, A. V. Georgiades. Asymptotic homogenization modeling and analysis of effective properties of smart composite reinforced and sandwich shells. Int. J. Mech. Sci., vol. 49, no.2, pp. 138-150, 2007.

[26]. P. Cartraud, T. Messager. Computational homogenization of periodic beam-like structures. Int. J. Solids. Struct., vol. 43, no. 3-4, pp. 686-696, 2006.

[27]. F. Ménard, P. Cartraud. Solid and 3D beam finite element models for the nonlinear elastic analysis of helical strands within a computational homogenization framework. Comput. Struct., vol. 257, pp. 106675, 2021.

[28]. G. D. Cheng, Y. W. Cai, L. Xu. Novel implementation of homogenization method to predict effective properties of periodic materials. Acta. Mech. Sinica-PRC, vol. 29, no. 4, pp. 550-556, 2013.

[29]. Y. W. Cai, L. Xu, G. D. Cheng. Novel numerical implementation of asymptotic homogenization method for periodic plate structures. Int. J. Solids. Struct., vol. 51, no. 1, pp. 284-292, 2014.

[30]. S. N. Yi, L. Xu, G. D. Cheng, Y. W. Cai. FEM formulation of homogenization method for effective properties of periodic heterogeneous beam and size effect of basic cell in thickness direction. Comput. Struct., vol. 156, pp. 1-11, 2015.

[31]. J. Yan, B. Zhou, Z. Yang, L. Xu, H. Hu. Mechanism exploration and effective analysis method of shear effect of helically wound structures. Finite. Elem. Aanl. Des., vol. 212, pp. 103840, 2022.

[32]. J. Huo, N. van Dijk, E. K. Gamstedt. Elastic properties of rhombic mesh structures based on computational homogenisation. Eng. Struct., vol. 172, pp. 66-75, 2018.

[33]. N. Buannic, P. Cartraud. Higher-order effective modeling of periodic heterogeneous beams. I. Asymptotic expansion method. Int. J. Solids. Struct., vol. 38, no. 40-41, pp. 7139-7161, 2001.

[34]. F. Treyssede, P. Cartraud. A two-dimensional formulation for the homogenization of helical beam-like structures under bending loads. Int. J. Solids. Struct., vol. 234, pp. 111270, 2022.

[35]. M. K. Ferradi, X. Cespedes. A curved beam model with the asymptotic expansion method. Eng. Struct., vol. 241, pp. 112494, 2021.

[36]. M. K. Ferradi, A. Lebée, A. Fliscounakis, X. Cespedes, K. Sab. A model reduction technique for beam analysis with the asymptotic expansion method. Comput. Struct., vol. 172, pp. 11-28, 2016.

[37]. Z. W. Huang, Y. F. Xing, Y. H. Gao. A two-scale asymptotic expansion method for periodic composite Euler beams. Compos. Struct., vol. 241, pp. 112033, 2020.

[38]. V. Berdichevsky, E. Armanios, A. Badir. Theory of anisotropic thin-walled closed-cross-section beams. Composites Engineering, vol. 2, no. 5-7, pp. 411-432, 1992.

[39]. V. V. Volovoi, D. H. Hodges, V. L. Berdichevsky, V. G. Sutyrin. Asymptotic theory for static behavior of elastic anisotropic I-beams. Int. J. Solids. Struct., vol. 36, no.7, pp. 1017-1043, 1999.

[40]. W. Yu. Simplified formulation of mechanics of structure genome. AIAA Journal, vol. 57, no. 10, pp. 4201-4209, 2019.

[41]. N. Liu, W. Yu. Evaluation of smeared properties approaches and mechanics of structure genome for analyzing composite beams. Mech. Adv. Mater. Struct., vol. 25, no. 14, pp. 1171-1185, 2018.

[42]. X. Liu, W. Yu. A novel approach to analyze beam-like composite structures using mechanics of structure genome. Adv. Eng. Softw., vol. 100, pp. 238-251,2016.

[43]. H. Niknam, A. H. Akbarzadeh. In-plane and out-of-plane buckling of architected cellular plates: Numerical and experimental study. Compos. Struct., vol. 206, pp. 739-749, 2018.

[44]. H. Niknam, A. H. Akbarzadeh. Thermo-mechanical bending of architected functionally graded cellular beams. Compos. Part. B-Eng., vol. 174, pp. 107060, 2019.

[45]. X. Liu, L. Gao, M. Xiao, Y. Zhang. Kriging-assisted design of functionally graded cellular structures with smoothly-varying lattice unit cells. Comput. Method. Appl. M., vol. 390, pp. 114466, 2022.

[46]. G. Savio, R. Meneghello, G. Concheri. Design of variable thickness triply periodic surfaces for additive manufacturing. Prog. Addit. Manuf., vol. 4, no. 3, pp. 281-290, 2019.

[47]. Y. Zhu, S. Li, Z. Du, C. Liu, X. Guo, W. Zhang. A novel asymptotic-analysis-based homogenisation approach towards fast design of infill graded microstructures. J. Mech. Phys. Solids., vol. 124, pp. 612–33, 2019.

[48]. C. Ma, D. Xue, S. Li, Z. Zhou, Y. Zhu, X. Guo. Compliance minimisation of smoothly varying multiscale structures using asymptotic analysis and machine learning. Comput. Method. Appl. M., vol. 395, pp. 114861, 2022.

[49]. L. Xu, D. Zhang, Y. Zhang, Y. Liang, Z. Qian. Effective property calculation and its numerical implementation of spatially graded plate structures based on asymptotic homogenization. Compos. Struct., vol. 300, pp. 116165, 2022.

[50]. D. Allman. A compatible triangular element including vertex rotations for plane elasticity analysis. Comput. Struct., vol. 19, no. 1-2, pp. 1-8, 1984.

[51]. M. Huang, Z. Zhao, C. Shen. An effective planar triangular element with drilling rotation. Finite. Elem. Anal. Des., vol. 46 ,no. 11, pp. 1031-1036, 2010.

[52]. J. C. Simo, M. Rifai. A class of mixed assumed strain methods and the method of incompatible modes. Int. J. Numer. Meth. Eng., vol. 29, no.8, pp. 1595-1638, 1990.